

Modeling the modulation of neuronal bursting: a singularity theory approach*

Alessio Franci^{1,*}, Guillaume Drion^{2,3}, & Rodolphe Sepulchre^{2,4}

¹ INRIA Lille-Nord Europe, Orchestron project, 40 avenue Halley F 59650
Villeneuve d'Ascq, France

² Department of Electrical Engineering and Computer Science, University of Liege, Liege, Belgium

³ Laboratory of Neurophysiology, GIGA Neurosciences, University of Liege, Liege, Belgium

⁴ University of Cambridge, Department of Engineering, Trumpington Street,
Cambridge CB2 1PZ, United Kingdom

* Corresponding author. Email: alessio.franci@inria.fr

Abstract

Exploiting the specific structure of neuron conductance-based models, the paper investigates the mathematical modeling of neuronal bursting modulation. The proposed approach combines singularity theory and geometric singular perturbations to capture the geometry of multiple time-scales attractors in the neighborhood of high-codimension singularities. We detect a three-time scale bursting attractor in the universal unfolding of the winged cusp singularity and discuss the physiological relevance of the bifurcation and unfolding parameters in determining a physiological modulation of bursting. The results suggest generality and simplicity in the organizing role of the winged cusp singularity for the global dynamics of conductance based models.

1 Introduction

Bursting is an important signaling component of neurons, characterized by a periodic alternation of bursts and quiescent periods. Bursts are transient, but high-frequency trains of spikes, contrasting with the absence of spikes during the quiescent periods. Bursting activity has been recorded in many neurons, both in vitro and in vivo, and electrophysiological recordings show a great variety of bursting time series. All neuronal bursters share nevertheless a sharp separation between three different time scales: a fast time-scale for the spike generation, a slow time-scale for the intraburst spike frequency, and an ultra slow time-scale for the inter burst frequency. Many neuronal models exhibit bursting in some parameter range and many bursting models have been analyzed through bifurcation theory but the exact mechanisms modulating neuronal bursting are still poorly understood, both mathematically and physiologically. In particular, modeling the route to burst, that is the physiologically observed modulation from a regular pacemaking activity to a bursting activity, has remained elusive to date. Also many efforts have been devoted at classifying different types of bursters ?????. But the mathematical mechanisms that allow a same neuron to be modulated across different types are rarely studied, despite their physiological role in homeostatic cell regulation and development ?.

*This paper presents research results of the Belgian Network DYSCO (Dynamical Systems, Control, and Optimization), funded by the Interuniversity Attraction Poles Programme, initiated by the Belgian State, Science Policy Office. The scientific responsibility rests with its authors.

As an attempt to advance the mathematical understanding of neuronal bursting, the present paper exploits the particular structure of conductance based neuronal models to address with a local analysis tool the global structure of bursting attractors. Rooted in the seminal work of Hodgkin and Huxley ?, conductance-based models are nonlinear RC circuits consisting of one capacitance (modeling the cell membrane) in parallel with possibly many voltage sources with voltage dependent conductance (each modeling a specific ionic current). The variables of the model are the membrane potential (V) and the gating (activation and inactivation) variables that model the kinetics of each ion channel. The vast diversity of ion channels involved in a particular neuron type leads to high-dimensional models, but all conductance-based models share two central structural assumptions:

- (i) a classification of gating variables in three well separated time-scales (fast variables - in the range of the membrane potential time scale $\sim 1ms$; slow variables - 5 to 10 times slower; and ultra-slow variables - 10 to hundreds time slower), which roughly correspond to the three time scales of neuronal bursting.
- (ii) each voltage regulated gating variable x obeys the first-order monotone dynamics $\tau_x(V)\dot{x} = -x + x_\infty(V)$, which implies that, at steady state, every voltage regulated gating variable is an explicit monotone function of the membrane potential, that is, $x = x_\infty(V)$.

Our analysis of neuronal bursting rests on these two structural assumptions. Assumption (i) suggests a three-time scale singularly perturbed bursting model, whose singular limit provides the skeleton of the bursting attractor. Assumption (ii) implies that the equilibria of arbitrary conductance-based models are determined by Kirchoff's law (currents sum to zero in the circuit), which provides a single algebraic equation in the sole scalar variable V . This remarkable feature calls for singularity theory ? to understand the equilibrium structure of the model.

The results of jointly exploiting timescale separation and singularity theory for neuronal bursting modeling provide the following specific contributions:

- The universal unfolding of the winged-cusp singularity is shown to organize a three time-scale burster. The three level hierarchy of singularity theory dictates the hierarchy of timescales: the state variable of the bifurcation problem is the fast variable, the bifurcation parameter is the slow variable, and unfolding parameter(s) are the ultra-slow variable(s). Because the geometric construction is grounded in the algebraic and timescale structure of conductance-based models, the proposed model can be related to detailed conductance-based models through mathematical reduction. We provide general conditions for this mathematical model to be a normal form reduction of an arbitrary conductance-based model. Both the bifurcation parameter and the unfolding parameters have a clear physiological interpretation.

- The bifurcation parameter is directly linked to the balance between restorative and regenerative slow ion channels, the importance of which was recently studied by the authors in ?. The modulation of the bifurcation parameter in the proposed three-time scale model provides a geometrically and physiologically meaningful transition from slow tonic spiking to bursting. This "route to bursting" is known to play a significant role in central nervous system activity ????. Its mathematical modeling appears to be novel.

- The three unfolding parameters modulate in an even slower scale the fast-slow phase portrait of the three-time scale burster. The affine parameter plays the classical role of an adaptation current that hysterically modulates the slow-fast phase portrait across a parameter range where a stable resting state and a stable spiking limit cycle coexist, thereby creating the bursting attractor. The two remaining unfolding parameters can modulate the bursting attractor across a continuum of bursting types. As a result, transition between differentiating bursting waveforms, observed for instance in developing neurons ?, are geometrically captured as paths in the unfolding space of the winged cusp. The physiological interpretation of this modulation is a straightforward consequence of the clear physiological interpretation of each unfolding parameter.

The existence of three-time scale bursters in the abstract unfolding of a winged cusp is presented in Section 2. Section 3 focuses on a minimal reduced model of neuronal bursting and uses the insight of singularity theory to describe a physiological route to bursting in this model. Section 4 shows how to trace the same geometry in arbitrary conductance based models. Section 5 discuss in a less technical way the relevance of the winged-cusp singularity for the modeling of bursting modulation. The technical details of mathematical proofs are presented in an appendix.

2 Universal unfolding and multi-time scale attractors

2.1 A primer on singularity theory

We introduce here some notation and terminology that will be used extensively in the paper. The interested reader is referred to the main results of Chapters I-IV in ? for a comprehensive exposition of the singularity theory used in this paper.

Singularity theory studies scalar bifurcation problems of the form

$$g(x, \lambda) = 0, \quad x, \lambda \in \mathbb{R}, \quad (1)$$

where g is a smooth function. The variable x denotes the state and λ is the bifurcation parameter. The set of pairs (x, λ) satisfying (1) is called the *bifurcation diagram*. *Singular points* satisfy $g(x^*, \lambda^*) = \frac{\partial g}{\partial x}(x^*, \lambda^*) = 0$. Indeed, if $\frac{\partial g}{\partial x}(x^*, \lambda^*) \neq 0$, then the implicit function theorem applies and the bifurcation diagram is necessarily regular at (x^*, λ^*) .

Except for the fold $x^2 \pm \lambda = 0$, bifurcations are not generic, that is they do not persist under small perturbations. Singularity theory is a robust bifurcation theory: it aims at classifying all possible persistent bifurcation diagrams that can be obtained by small perturbations of a given singularity.

A *universal unfolding* of $g(x, \lambda)$ is a parametrized family of functions $G(x, \lambda; \alpha)$, where α lies in the unfolding parameter space \mathbb{R}^k , such that

- 1) $G(x, \lambda; 0) = g(x, \lambda)$
- 2) Given any $p(x)$ and a small $\mu > 0$, one can find an α near the origin such that the two bifurcation problems $G(x, \lambda; \alpha) = 0$ and $g(x, \lambda) + \mu p(x) = 0$ are qualitatively equivalent.
- 3) k is the minimum number of unfolding parameters needed to reproduce all perturbed bifurcation diagrams of $g(x, \lambda)$. k is called the codimension of $g(x, \lambda)$.

Unfolding parameters are not bifurcation parameters. Instead, they change the qualitative bifurcation diagram of the perturbed bifurcation problem $G(x, \lambda; \alpha) = 0$. That is why λ is a distinguished parameter in the theory. Historically, this parameter was associated to a slow time, whose evolution lets the dynamics visit the bifurcation diagram in a quasi-steady state manner. It will play the same role in the present paper, where we only consider two singularities and their universal unfolding:

the codimension 1 hysteresis

$$g_{hy}^s(x, \lambda) = -x^3 - \lambda, \quad (2)$$

whose universal unfolding is shown to be (?, Chapter IV)

$$G_{hy}^s(x, \lambda; \beta) = -x^3 - \lambda + \beta x, \quad (3)$$

the codimension 3 winged cusp

$$g_{wcusp}^s(x, \lambda) = -x^3 - \lambda^2, \quad (4)$$

whose universal unfolding is shown to be (?, Section III.8 and Chapter IV)

$$G_{wcusp}^s(x, \lambda; \alpha, \beta, \gamma) = -x^3 - \lambda^2 + \beta x - \gamma \lambda x - \alpha. \quad (5)$$

The universal unfolding of codimension ≥ 1 bifurcations contains some codimension 1 bifurcation. For instance, the universal unfolding of the winged cusp possesses hysteresis bifurcations on the unfolding parameter hypersurface defined by $\alpha\gamma^2 + \beta = 0$, $\alpha \leq 0$. Even though such bifurcation diagrams are not persistent, they define *transition varieties* that separate equivalence classes of persistent bifurcation diagrams, hence, providing a complete classification of persistent bifurcation diagrams.

An unperturbed bifurcation problem assumes the suggestive role of *organizing center*: all the perturbed bifurcation diagrams are determined and organized by the unperturbed bifurcation diagram, which constitutes the most singular situation. Via the inspection of local algebraic conditions at the singularity, an organizing center provides a quasi-global description of all possible perturbed bifurcation diagrams.

2.2 The hysteresis singularity and spiking oscillations

The hysteresis singularity has a universal unfolding $-x^3 - \lambda + \beta x$ with persistent bifurcation diagram plotted in Figure 1A for $\beta > 0$. We use this algebraic curve to generate the phase portrait in Fig. 1B of the two-time scale model

$$\dot{x} = G_{hy}^s(x, \lambda + y; \beta) \quad (6a)$$

$$\begin{aligned} &= -x^3 + \beta x - \lambda - y \\ \dot{y} &= \varepsilon(x - y) \end{aligned} \quad (6b)$$

Because y is a slow variable, it acts as a slowly varying modulation of the bifurcation

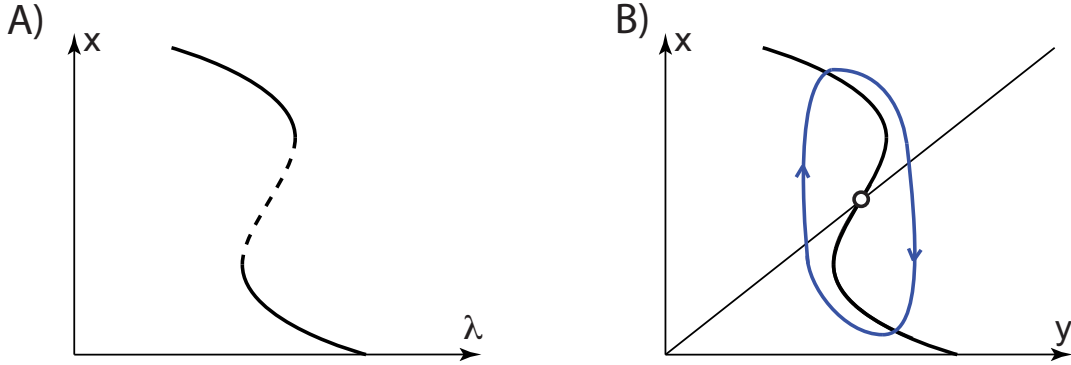


Figure 1: **Relaxation oscillations in the universal unfolding of the hysteresis bifurcation.** **A.** A persistent bifurcation diagram of the hysteresis singularity. Branches of stable (resp. unstable) fixed points are depicted as full (resp. dashed) lines. **B.** Through a slow adaptation of the bifurcation parameter, the bifurcation diagram in A. is transformed into the phase plane of a two-dimensional dynamical system, which still defines a universal unfolding of the hysteresis singularity. The thick full line is the fast subsystem nullcline. The thin full line is the slow subsystem nullcline. The circle denotes an unstable fixed point. For small $\beta > 0$, the model exhibits exponentially stable relaxation oscillations (depicted in light blue).

parameter in the fast dynamics (6a). As a consequence, the global analysis of system (6) reduces to a quasi-steady state bifurcation analysis of (6a), hence the relationship between Fig. 1A and Figure 1B.

The following (well known) theorem characterizes a global attractor of (6), that is the existence of Van-der-Pol type relaxation oscillations in the universal unfolding of the hysteresis.

Theorem 1 *For $\lambda = 0$ and for all $0 < \beta < 1$, there exists $\bar{\varepsilon} > 0$ such that, for all $\varepsilon \in (0, \bar{\varepsilon}]$, the dynamical system (6) possesses an exponentially stable relaxation limit cycle, which attracts all solutions except the equilibrium at $(0, 0)$.*

The familiar reader will recognize in (6) a famous model of neurodynamics introduced by FitzHugh ? . It is the prototypical planar reduction of spiking oscillations. There is therefore a close relationship between the hysteresis singularity and spike generation.

It is worth emphasizing that the relationship between singularity theory (Fig. 1A) and the two-time scale phase portrait (Fig. 1B) imposes choosing the bifurcation parameter, not an unfolding parameter, as the slow variable. It should also be observed that the slow variable is a deviation from the unfolding parameter λ rather than the bifurcation parameter itself. Keeping λ as the bifurcation parameter of the two-dimensional dynamics (6) allows to shape its equilibrium structure accordingly to the universal unfolding of the organizing singularity, in this case, the hysteresis, and will play an important role in the next section.

2.3 The winged cusp singularity and rest-spike bistability

We repeat the elementary construction of Section 2.2 for the codimension-3 winged cusp singularity $-x^3 - \lambda^2$. It differs from the hysteresis singularity in the *non-monotonicity* of $g(x, \lambda)$ in the bifurcation parameter, that is $\frac{\partial(-x^3 - \lambda^2)}{\partial \lambda} = -2\lambda$ changes sign at the singularity.

Figure 2A illustrates an important persistent bifurcation diagram in the unfolding of the winged cusp, obtained for $\gamma = 0$, $\beta > 0$, and $\alpha < -2\left(\frac{\beta}{3}\right)^{3/2}$. We call it the *mirrored hysteresis* bifurcation diagram. The right part ($\lambda > 0$) of this bifurcation diagram is essentially the persistent bifurcation diagram of the hysteresis singularity in Figure 1A. In that region, $\frac{\partial G_{wcusp}^s}{\partial \lambda} < 0$. The left part ($\lambda < 0$) is the mirror of the hysteresis and, in that region, $\frac{\partial G_{wcusp}^s}{\partial \lambda} > 0$. For $\gamma \neq 0$, the mirroring effect is not perfect, but the qualitative analysis does not change. The hysteresis and its mirror collide in a transcritical singularity for $\alpha = -2\left(\frac{\beta}{3}\right)^{3/2}$. This singularity belongs to the transcritical bifurcation transition variety in the winged cusp unfolding (see Appendix A). The transcritical bifurcation variety plays an important role in the forthcoming analysis.

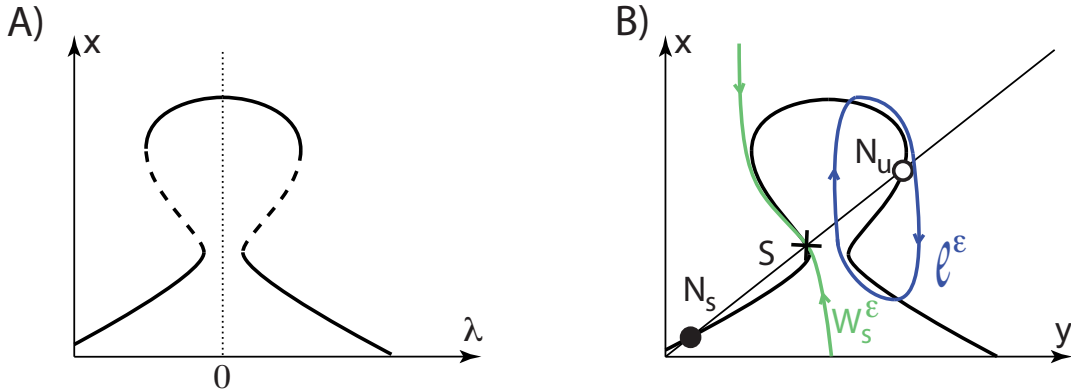


Figure 2: **Singularly perturbed rest-spike bistability in the universal unfolding of the winged cusp.**
A. *Mirrored hysteresis* persistent bifurcation diagram of the winged cusp for $\beta > 0$, $\alpha < -2\left(\frac{\beta}{3}\right)^{3/2}$, and $\gamma = 0$.
B. A phase plane of (7).

We use the algebraic curve in Figure 2A to generate the phase portrait in Figure 2B of the two-dimensional model

$$\dot{x} = G_{wcusp}^s(x, \lambda + y; \alpha, \beta, \gamma) \quad (7a)$$

$$\begin{aligned} &= -x^3 + \beta x - (\lambda + y)^2 - \gamma(\lambda + y)x - \alpha \\ \dot{y} &= \varepsilon(x - y). \end{aligned} \quad (7b)$$

Its fixed point equation

$$F(x, \lambda, \alpha, \beta, \gamma) := -x^3 + \beta x - (\lambda + x)^2 - \gamma(\lambda + x)x - \alpha. \quad (8)$$

is easily shown to be again a universal unfolding of the winged cusp around $x_{wusp} := \frac{1}{3}$, $\lambda_{wusp} := 0$, $\alpha_{wusp} := -\frac{1}{27}$, $\beta_{wusp} := -\frac{1}{3}$, $\gamma_{wusp} := -2$. The face portrait in Fig. 2B is a prototype phase portrait of rest-spike bistability: a stable fixed point coexists with a stable relaxation limit cycle.

Similarly to the previous section, the analysis of the singularly perturbed model (7) is completely characterized by the bifurcation diagram of Figure 2A. This bifurcation diagram provides a skeleton for the rest-spike bistable phase portrait in Figure 2B, as stated in the following theorem. Its proof is provided in Section B.1.

Theorem 2 *For all $\beta > \beta_{wusp}$, there exist open sets of bifurcation (λ) and unfolding (α, γ) parameters near the pitchfork singularity at $(\lambda, \alpha, \gamma) = (\lambda_{PF}(\beta), \alpha_{PF}(\beta), \gamma_{PF}(\beta))$, in which, for sufficiently small $\varepsilon > 0$, model (7) exhibits the coexistence of an exponentially stable fixed point N_s and an exponentially stable spiking limit cycle ℓ^ε . Their basins of attraction are separated by the stable manifold W_s^ε of a hyperbolic saddle S (see Fig. 2B).*

Figure 3 shows the transition in (7) from the hysteresis phase portrait in Figure 1B to the bistable phase portrait in Fig. 2B through a transcritical bifurcation. Both phase portraits are generated by unfolding the degenerate portrait in Fig. 3, center, which belongs to the pitchfork bifurcation variety $(\alpha, \gamma) = (\alpha_{PF}(\beta), \gamma_{PF}(\beta))$, $\beta > \beta_{wusp}$ (see Appendix A). The transcritical bifurcation variety $\alpha = \alpha_{TC}(\beta, \gamma)$ is obtained through variations of the unfolding parameter γ away from the pitchfork variety. It provides the two phase portraits in Fig. 3, center top and bottom. By increasing or decreasing the bifurcation parameter λ and decreasing the unfolding parameter α out of the transcritical bifurcation variety, these phase portraits perturb to the generic phase portraits in the corner, corresponding to the qualitative phase portraits in Figures 1B and Fig. 2B, respectively. The reader of ? will recognize the same organizing role of the pitchfork in a planar model of neuronal excitability.

2.4 A three-time scale bursting attractor in the winged cusp unfolding

The coexistence of a stable resting state and stable spiking oscillation, or *singularly perturbed rest-spike bistability*, makes (7) a good candidate as the slow-fast subsystem of a three-time scale minimal bursting model:

$$\dot{x} = G_{wusp}^s(x, \lambda + y; \alpha + z, \beta, \gamma) \quad (9a)$$

$$= -x^3 + \beta x - (\lambda + y)^2 - \gamma(\lambda + y)x - \alpha - z$$

$$\dot{y} = \varepsilon_1(x - y) \quad (9b)$$

$$\dot{z} = \varepsilon_2(-z + ax + by + c), \quad (9c)$$

where $0 < \varepsilon_2 \ll \varepsilon_1 \ll 1$ and $a, b, c \in \mathbb{R}$. The z -dynamics models the ultra-slow adaptation of the affine unfolding parameter α , in such a way that the global attractor of (9) will be determined by a quasi-static modulation of (9a) through different persistent bifurcation diagrams.

Here, again, the role of singularity theory in distinguishing bifurcation and unfolding parameters is crucial. The hierarchy between these parameters and the state variable, formalized in the theory in (?, Definition III.1.1), is reflected here in the hierarchy of timescales.

The time scale separation between (9a-9b) and (9-c) makes it possible once again to derive a global analysis of model (9) from the analysis of the steady state behavior of (7) as α is varied. Such analysis can easily be derived geometrically in the singular limit

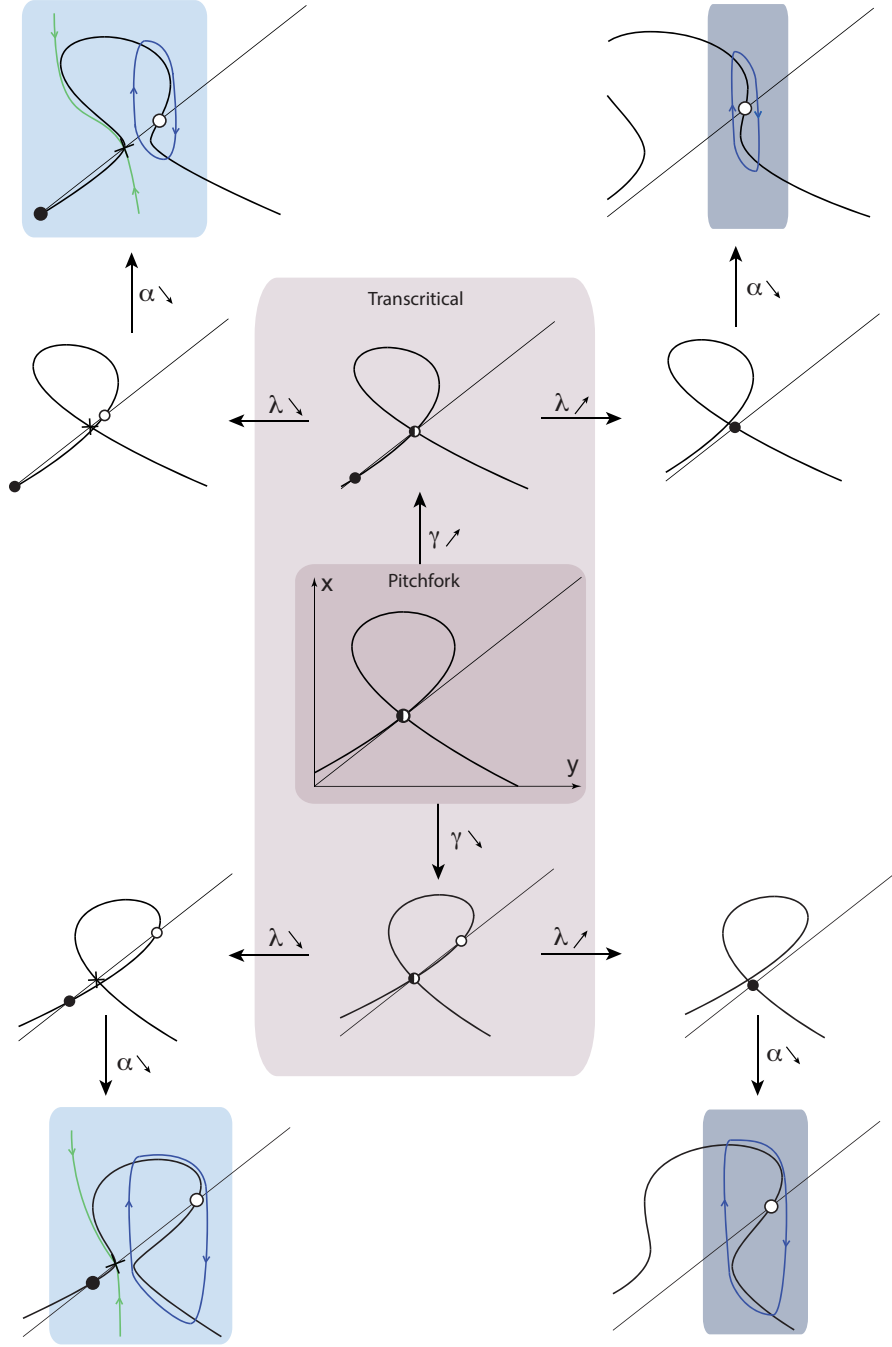


Figure 3: **An unfolding of the pitchfork bifurcation variety in (7).** The phase portraits in Figs. 1 and 2 both belong to the unfolding of the pitchfork singularity in center. A smooth deformation of the phase portrait of Fig. 1 into the phase portrait of Fig. 2 involves a transcritical bifurcation, which degenerate into a pitchfork for a particular value of the unfolding parameter γ

$\varepsilon_1 = 0$. It is sketched in Figure 4. For $\alpha \in (\alpha_{SN}, \alpha_{SH}^0)$, the singularly perturbed model (7) exhibits rest-spike bistability, that is, the coexistence of a stable node N_s , a singular stable periodic orbit ℓ^0 , and a singular saddle separatrix W_s^0 . At $\alpha = \alpha_{SH}^0 = -2 \left(\frac{\beta}{3} \right)^{3/2}$ the left and right branches of the mirrored hysteresis bifurcation collide in a transcritical

singularity that serves as a connecting point for a singular homoclinic trajectory SH^0 . For $\alpha > \alpha_{SH}^0$, the only (singular) attractor is the stable node N_s . At $\alpha = \alpha_{SN}$, the saddle and the stable node merge in a saddle-node bifurcation SN . For $\alpha < \alpha_{SN}$, the only attractor is the singular periodic orbit ℓ^0 . The different singular invariant sets in Figure 4A, can be glued together to construct the three-dimensional singular invariant set \mathcal{M}_0 in Figure 4B-left.

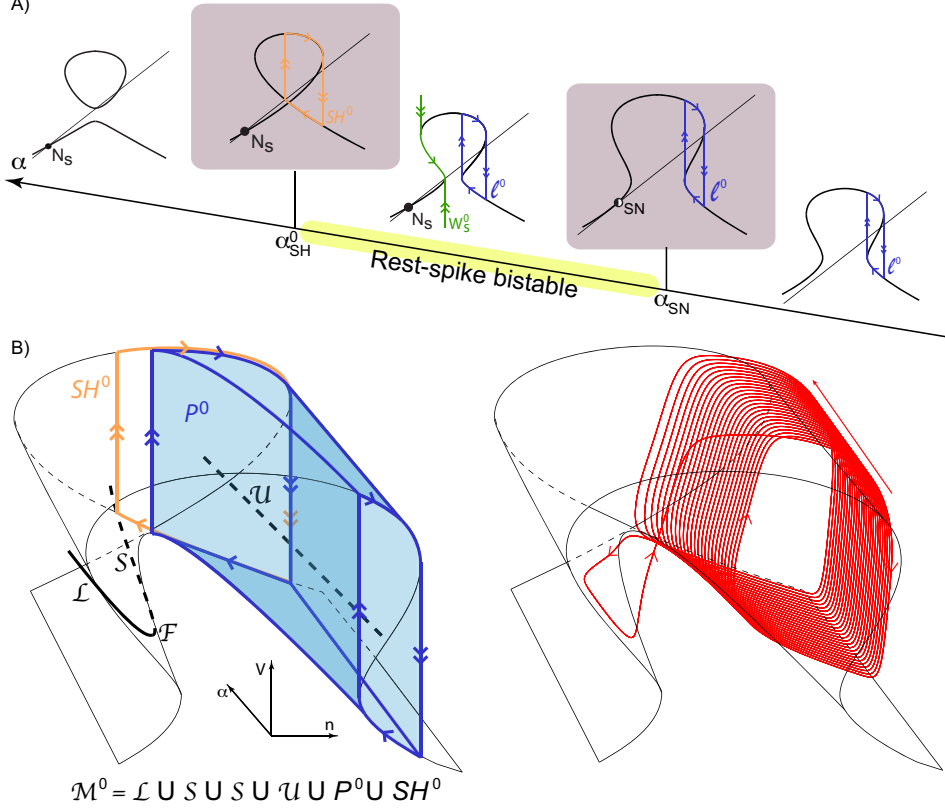


Figure 4: **Singular steady-state behavior of (7) through a variation of the unfolding parameter α .** **A.** Singular phase portraits of (7) for $\gamma = 0$, $\beta = \frac{1}{3}$, and small negative λ . **B.** Gluing the different invariant sets in **A** leads to the three-dimensional singular invariant set \mathcal{M}^0 (left), which provides a skeleton for a three-time scale bursting attractor (right) in the singularly perturbed system (9). The branch of stable fixed points (resp. saddle point) for $\alpha < \alpha_{SN}$ is drawn as the black solid curve \mathcal{L} (resp. the black dashed curve \mathcal{S}). The saddle node bifurcation connecting them is denoted by \mathcal{F} . The branch of unstable fixed points is drawn as the black dashed line \mathcal{U} . The branch of stable singular periodic orbit for $\alpha < \alpha_{SH}^0$ is drawn as the blue cilindric surface P^0 . The singular saddle homoclinic trajectory is drawn as the orange oriented curve SH^0 .

The singular invariant set \mathcal{M}_0 provides a skeleton for a three-time scale bursting attractor that shadows the branch \mathcal{L} of stable fixed points in alternation with the branch P^0 of (singular) stable periodic orbits, as depicted in Figure 4B-right. To prove the existence of such an attractor, we only need to understand how \mathcal{M}^0 perturbs for $\varepsilon_1 > 0$.

Near the singular limit, the branch of singular periodic orbits P^0 perturbs to a nearby branch of exponentially stable periodic orbits P^ε (see Fig. 5), whereas the singular homoclinic trajectory SH^0 perturbs to an unstable homoclinic trajectory SH^ε (at $\alpha = \alpha_{SH}^\varepsilon$). The branch of unstable periodic orbits Q^ε generated at SH^ε eventually merges with P^ε at a fold limit cycle bifurcation \mathcal{F}_{LC} for some $\alpha_{FLC}^\varepsilon \in (\alpha_{SH}^\varepsilon, \alpha_{SH}^0)$. In the whole range $(\alpha_{SN}, \alpha_{FLC}^\varepsilon)$, model (7) exhibits the coexistence of a stable fixed point and a stable spiking limit cycle. The details of this analysis are contained in Lemma 3 in Section B.2.

We follow ?? to derive conditions on the bifurcation and unfolding parameters in (9a-9b) and to place the hyperplane $\dot{z} = 0$ (through a suitable choice of the parameters

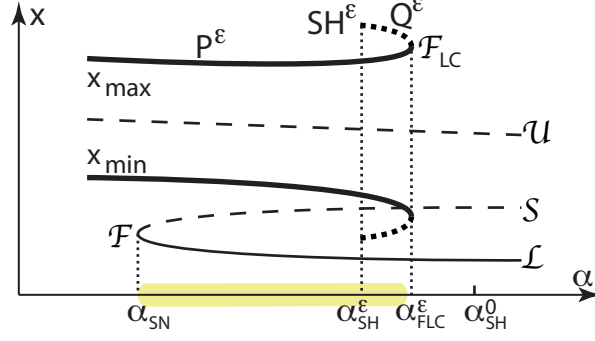


Figure 5: **Bifurcation diagram of (7) with respect the unfolding parameter α for sufficiently small ε .** The branch of stable fixed point is depicted as the full thin line \mathcal{L} , the branch of saddle point as the dashed thin line \mathcal{S} , and the branch of unstable fixed point as the dashed thin line \mathcal{U} . The branch of stable periodic orbit is depicted by the thick full lines P^ε and the branch of unstable periodic orbits by the thick dashed lines Q^ε . SH^ε : saddle-homoclinic bifurcation. F_{LC} : fold limit cycle bifurcation. F : fold (saddle-node) bifurcation. The yellow strip between the saddle-node and fold limit cycle bifurcation denotes the rest-spike bistable range.

$a, b, c \in \mathbb{R}$) such that an ultra-slow variation of z can hysteretically modulate the slow-fast subsystem (9a-9b) across its bistable range $(\alpha_{SN}, \alpha_{FLC}^\varepsilon)$ to obtain stable bursting oscillations. The existence of such bursting oscillations is stated in the following theorem. Its proof is provided in Section B.2.

Theorem 3 *For all $\beta > \beta_{wcusp}$, there exists an open set of bifurcation (λ) and unfolding (α, γ) parameters near the pitchfork singularity at $(\lambda, \alpha, \gamma) = (\lambda_{PF}(\beta), \alpha_{PF}(\beta), \gamma_{PF}(\beta))$ such that, for all λ, α, γ in those sets, there exist $a, b, c, \in \mathbb{R}$ such that, for sufficiently small $\varepsilon_1 \gg \varepsilon_2 > 0$, model (9) has a hyperbolic bursting attractor.*

Theorem 3 uses the two regenerative phase portraits in Fig. 3 left to construct a *bursting* attractor by modulating the unfolding parameter α . The bursting attractor directly rests upon the bistability of those phase portraits. It should be noted that the same construction can be repeated on the restorative phase portraits in Fig. 3 right. However those phase portraits are monostable and their ultra-slow modulation leads to a *slow tonic spiking* (*i.e.* a single spike necessarily followed by a rest period). This attractor differs from a bursting attractor by the absence of a bistable range in the bifurcation diagrams of Fig. 4. It can be shown that the persistence of (rest-spike) bistability in the singular limit is a hallmark of regenerative excitability (Fig. 3 left) and that it cannot exist in restorative excitability (Fig. 3 right). See ? for a more detailed discussion. Modulation in (9) of the bifurcation parameter across the transcritical bifurcation of Fig. 3 therefore provides a geometric transition from the slow tonic spiking attractor to the bursting attractor. This transition organizes the geometric route into bursting discussed in the next section.

3 A physiological route to bursting

3.1 A minimal three-time scale bursting model

The recent paper ? introduces the planar neuron model

$$\dot{V} = V - \frac{V^3}{3} - n^2 + I \quad (10a)$$

$$\dot{n} = \varepsilon(n_\infty(V - V_0) + n_0 - n) \quad (10b)$$

Its phase portrait was shown to contain the pitchfork of Figure 3 as an organizing center, leading to distinct types of excitability for distinct values of the unfolding parameters. The

analysis of the previous section suggests that a bursting model is naturally obtained by augmenting the planar model (10) with ultra slow adaptation:

$$\dot{V} = kV - \frac{V^3}{3} - (n + n_0)^2 + I - z \quad (11a)$$

$$\dot{n} = \varepsilon_n(V) (n_\infty(V - V_0) - n) \quad (11b)$$

$$\dot{z} = \varepsilon_z(V)(z_\infty(V - V_1) - z) \quad (11c)$$

Model (10) is essentially model (11) for $k = 1$ and $z = 0$, modulo a translation $n \leftarrow n + n_0$. The dynamics (11b-11c) mimic the kinetics of gating variables in conductance-based models, where the steady-state characteristics $n_\infty(\cdot)$ and $z_\infty(\cdot)$ are monotone increasing (typically sigmoidal) and the time scaling $\varepsilon_n(\cdot)$ and $\varepsilon_z(\cdot)$ are Gaussian-like strictly positive functions. Details of model (11) for the numerical simulations of the paper are provided in Appendix C.

The slow-fast subsystem (11a-11b) shares the same geometric structure as (7). After a translation $V \leftarrow V + V_0$, the right hand side of (11a) can easily be shown to be a universal unfolding of the winged cusp and the slow dynamics (11b) modulates its bifurcation parameter. Plugging the ultra-slow dynamics (11c), one recovers the same structure as (9). Therefore, the conclusions of Theorems 2 and 3 apply to (11).

The difference between (11) and (9) is that the model (11) has the physiological interpretation of a reduced conductance-based model, with V a fast variable that aggregates the membrane potential with all fast gating variables, n a slow recovery variable that aggregates all the slow gating variables regulating neuronal excitability, and z an ultra-slow adaptation variable that aggregates the ultra-slow gating variables that modulate the cellular rhythm over the course of many action potentials. Finally, I models an external applied current.

3.2 Model parameters and their physiological interpretation

The bifurcation parameter n_0 models the balance between restorative and regenerative ion channels

The central role of the bifurcation parameter n_0 in (11) was analyzed in ?? and is illustrated in Fig. 6. The transcritical bifurcation variety in Fig. 3 corresponds to the physiologically relevant transition from restorative excitability (large n_0) to regenerative excitability (small n_0). When the excitability is restorative, the recovery variable n provides negative feedback on membrane potential variations near the resting equilibrium, a physiological situation well captured by FitzHugh-Nagumo model (or the hysteresis singularity). In contrast, when excitability is regenerative, the recovery variable n provides positive feedback on membrane potential variations near the resting potential, a physiological situation that requires the quadratic term in (11a) (or the winged cusp singularity).

The value of n_0 in a conductance-based model reflects the balance between restorative and regenerative ion channels that regulate neuronal excitability. How to determine the balance in an arbitrary conductance-based model is discussed in ?. Note that the restorative or regenerative nature of a particular ion channel in the slow time-scale is an intrinsic property of the channel. A prominent example of restorative channel is the slow potassium activation shared by (almost) all spiking neurons. A prominent example of regenerative channel is the slow calcium activation encountered in most bursting neurons. The presence of regenerative channels in neuronal bursters is well established in neurophysiology. See e.g. ??.

The affine unfolding parameter provides bursting by ultra-slow modulation of the current across the membrane

For small n_0 , the modulation of the ultra-slow variable z creates a hyperbolic bursting attractor through the hysteretic loop described in Fig. 4. The burster becomes a single-

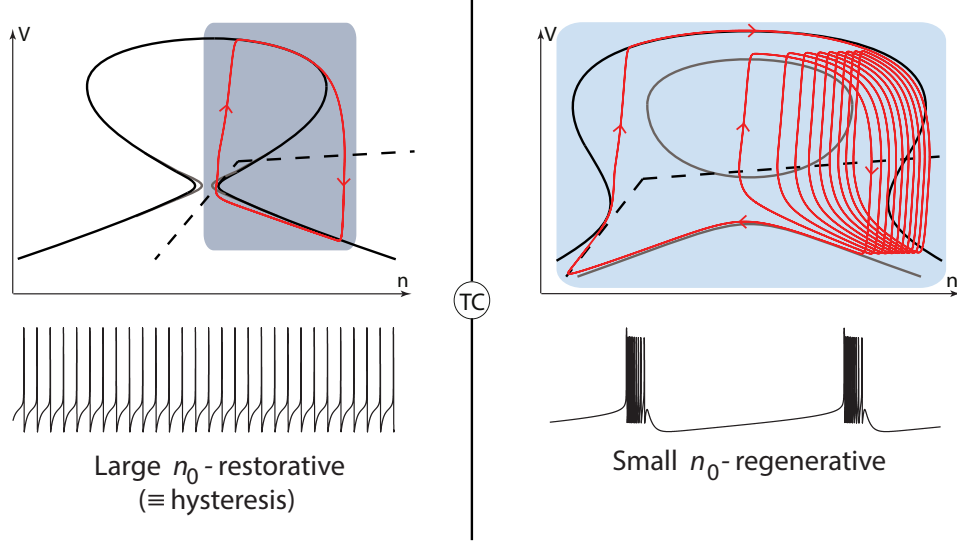


Figure 6: **Transition from restorative excitability (tonic firing) to regenerative excitability (bursting) in model (11) by sole variation of the bifurcation parameter n_0 .** The analytical expression of the steady state functions $n_\infty(\cdot)$ and $z_\infty(\cdot)$ and numerical parameter values are provided in Appendix C. The time scale is the same in the left and right time series.

spike limit cycle (tonic firing) for large n_0 (restorative excitability), that is, in the absence of rest-spike bistability in the planar model.

The presence of ultra-slow currents in neuronal bursters is well established in neurophysiology (see e.g. ?). A prominent example is provided by ultra-slow calcium activated potassium channels.

Half activation potential affects the route to bursting

The role of the unfolding parameter γ in (9) is illustrated in Fig. 3: it provides two qualitatively distinct paths connecting the restorative and regenerative phase portraits. This role is played by the parameter V_0 in the planar model (10) studied in ?, which has the physiological interpretation of a half activation potential. The role of half-activation potentials in neuronal excitability is well documented in neurophysiology (see e.g. ?). The role of this unfolding parameter in the route to bursting is discussed in the next subsection.

No spike without fast autocatalytic feedback

The role of the unfolding parameter k in (11) is to provide positive (autocatalytic) feedback in the fast dynamics. The prominent source of this feedback in conductance-based models is the fast sodium activation. It is well acknowledged in neurodynamics ?.

The reduced model (11) makes clear predictions about its dynamical behavior in the absence of this feedback (*i.e.* $k = 0$). Those predictions are further discussed in Section 5.2 and are in closed agreement with the experimental observation of “small oscillatory potentials” when sodium channels are shut down with pharmacological blockers ?? or are poorly expressed during neuronal cell development ?.

3.3 A physiological route to bursting

A central insight of the reduced model (11) is that it provides a route to bursting: fixing all unfolding parameters and varying only the bifurcation parameter n_0 leads to a smooth transition from tonic firing to bursting, see Fig. 7. Smooth and reversible transitions between those two rhythms have been observed in many experimental recordings ??, making

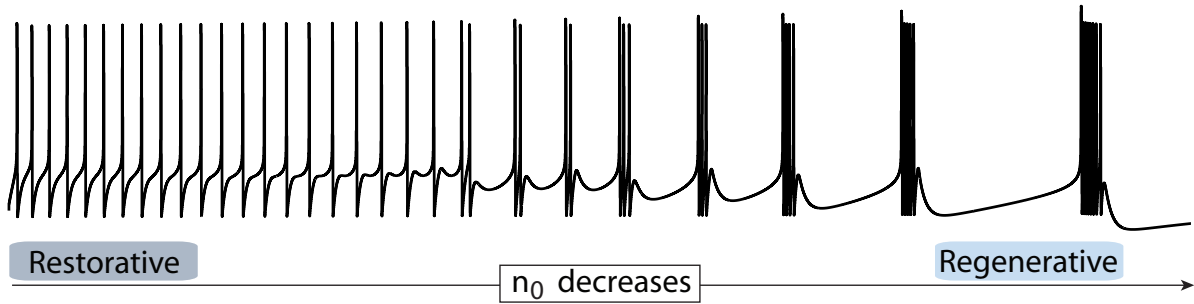


Figure 7: **Route from tonic firing to bursting in model (11) via a smooth variation of the bifurcation parameter n_0 .** Rest of the parameter as in Figure 6.

the route to burst an important signaling mechanism. The fact that the modulation is achieved simply through the bifurcation parameter n_0 , *i.e.* the balance between restorative and regenerative channels, is of physiological importance because it is consistent with the physiology of experimental observations of routes into bursting ???.

The analysis in the above sections shows that the transition from single spike to bursting is through the transcritical bifurcation variety in model (7). Looking at the singular limit $\varepsilon = 0$ of (7) near this transition variety provides further insight on the geometry of the route that leads to the appearance of the saddle-homoclinic bifurcation organizing the bistable phase-portrait. This route is organized by the path through the pitchfork bifurcation, which provides the most symmetric path across the transcritical variety. The generic transitions are understood by perturbing the degenerate path.

Fig. 8A shows the qualitative projection of those paths onto the (V_0, n_0) parameter chart obtained in model (10) for $I = \frac{2}{3}$. The chart is reproduced from ?. The same qualitative picture is obtained for the (γ, λ) parameter chart of the abstract model (7) at $\alpha = \alpha_{TC}(\beta, \gamma)$ (see Appendix A). The chart associates different excitability types (as well as their restorative or regenerative nature, see ?) to distinct bifurcation mechanisms. Unfolding those paths along the I (or α) direction leads to the bifurcation diagrams in Fig. 9B. They reveal (in the singular limit) the onset of the bistable range organized by the singular saddle-homoclinic loop SH^0 as paths cross the transcritical bifurcation variety.

The same qualitative picture persists for $\varepsilon > 0$. Fig. 9 illustrates how the appearance of the singular saddle-homoclinic loop is accompanied, for $\varepsilon > 0$, by a smooth transition from a monostable (SNIC - route *i*) or barely bistable (sub. Hopf - route *ii*) bifurcation diagram to the robustly bistable bifurcation diagram constructed in the sections above (Fig. 5). Through ultra-slow modulation of the unfolding parameter α , this transition geometrically captures the transition from tonic spiking to bursting via the sole variation of the bifurcation parameter.

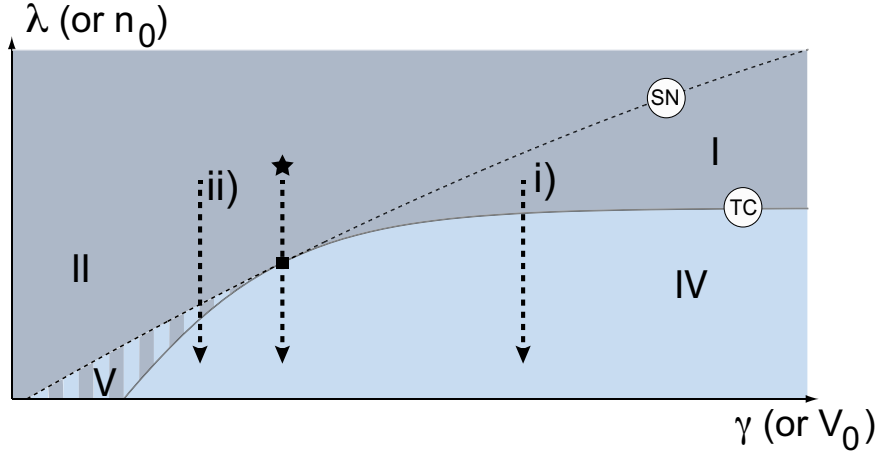
The strong agreement between the mathematical insight provided by singularity theory and the known electrophysiology of bursting is a peculiar feature of the proposed approach. There is a direct correspondence between the bifurcation and unfolding parameters of the winged cusp and the physiological minimal ingredients of a neuronal burster. In particular, our analysis predicts that any bursting neuron must possess at least one physiologically regulated slow regenerative channel. This prediction needs to be tested systematically but we have found no counter-example in the bursting neurons we have analyzed to date.

4 Normal form reduction of conductance-based models

4.1 A two dimensional reduction

The winged cusp singularity emerges as an organizing center of rhythmicity in the reduced neuronal model (11), but a legitimate question is whether this singularity can be traced in

A)



B)

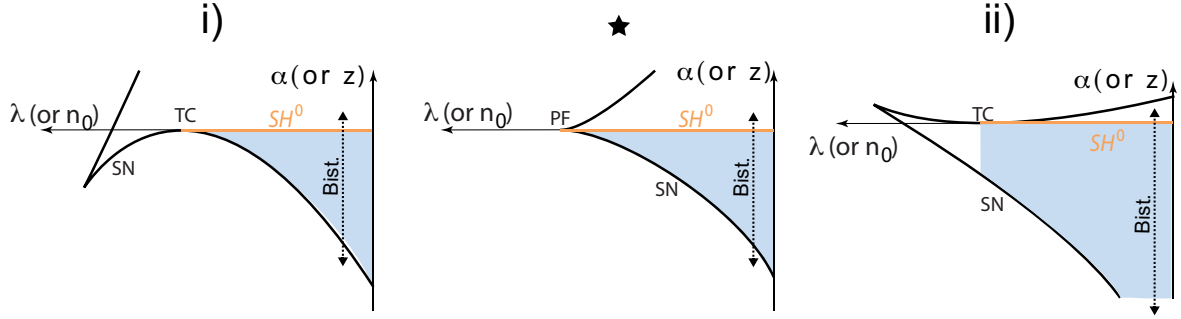


Figure 8: **Routes into bursting in the universal unfolding of the pitchfork bifurcation.** **A.** Qualitative projection of routes into bursting onto the (V_0, n_0) (resp. (γ, λ)) of model (10) (resp. (7)) for $I = \frac{2}{3}$ (resp. $\alpha = \alpha_{TC}(\beta, \gamma)$, see Appendix A). Excitability is restorative in subregions I and II, mixed in subregion V, and regenerative in subregion IV. See ? and ? for details concerning the underlying bifurcation mechanisms. The transition path labeled with a star depicts the degenerate path across the pitchfork. The generic paths i) and ii) are distinguished by different half activation potentials V_0 (resp. unfolding parameter γ). **B.** Unfolding of transition paths in A along the I (resp. α) direction. Black thick lines denote branches of saddle-node (SN) bifurcation. In paths i) and ii), the model undergoes a transcritical bifurcation (TC) as the path touches tangentially a branch of SN bifurcations. In the degenerate path, the model undergoes a pitchfork (PF) bifurcation as the path enters the cusp tangentially to both branches of SN bifurcations. The singular saddle-homoclinic loop, geometrically constructed in Figs. 4 and 9, is denoted by SH^0 and determines the appearance of a singular bistable range persisting away from singular limit.

arbitrary (high-dimensional) conductance-based models. Our recent paper ? addresses a closely related question for the transcritical variety. It provides an analog of the bifurcation parameter n_0 in arbitrary conductance-based models of the form

$$C_m \dot{V} = - \sum_{\iota} \bar{g}_{\iota} m_{\iota}^{a_{\iota}} h_{\iota}^{b_{\iota}} (V - E_{\iota}) + I_{app},$$

$$=: I_{ion}(V, x^f, x^s, x^{us}) + I_{app} \quad (12a)$$

$$\tau_{x_j^f}(V) \dot{x}_j^f = -x_j^f + x_{j,\infty}^f(V), \quad j = 1, \dots, n_f \quad (12b)$$

$$\tau_{x_j^s}(V) \dot{x}_j^s = -x_j^s + x_{j,\infty}^s(V), \quad j = 1, \dots, n_s \quad (12c)$$

$$\tau_{x_j^{us}}(V) \dot{x}_j^{us} = -x_j^{us} + x_{j,\infty}^{us}(V), \quad j = 1, \dots, n_{us} \quad (12d)$$

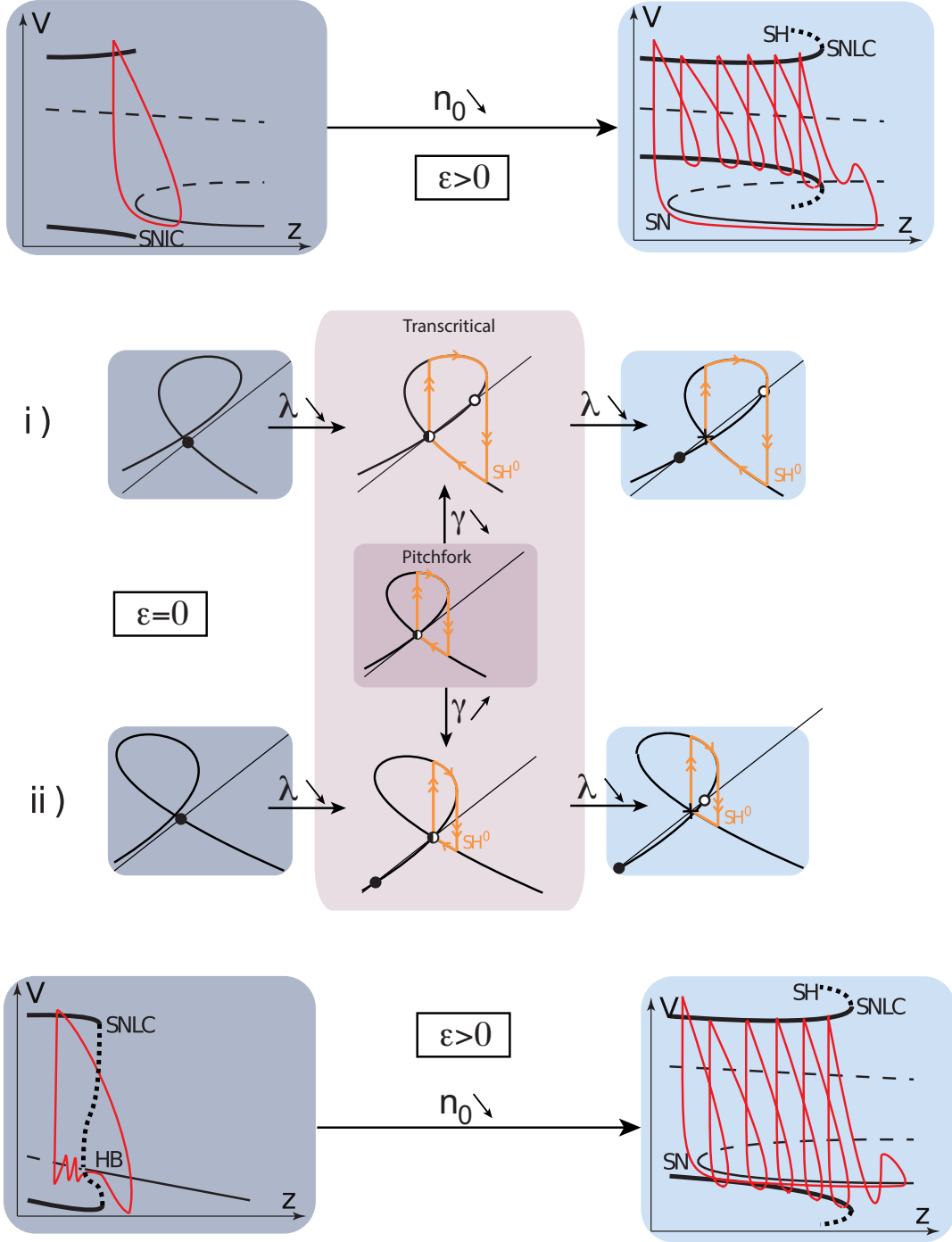


Figure 9: Geometry of the two generic routes into bursting in the unfolding of the pitchfork bifurcation in model (9) and model (11).

where ι runs through all ionic currents, $x^f := [x_j^f]_{j=1,\dots,n_f}$ denotes the n_f -dimensional column vector of fast gating variables, $x^s := [x_j^s]_{j=1,\dots,n_s}$ denotes the n_s -dimensional column vector of slow gating variables, and $x^{us} := [x_j^{us}]_{j=1,\dots,n_{us}}$ denotes the n_{us} -dimensional column vector of ultra-slow variables (see also ? for more details on the adopted notation).

Following common analysis methods in neurodynamics, we want to reduce the (possi-

bly) high-dimensional model (12) to a two-dimensional model of the form

$$\dot{V} = F(V, n) + I \quad (13a)$$

$$\tau(V)\dot{n}^s = -n + n_\infty^s(V) \quad (13b)$$

where V is the fast voltage and n is a slow aggregate variable. We achieve this reduction by first considering the singular limit of three time scales leading to a quasi-steady state approximation for fast gating variables, that is

$$x_j^f \equiv x_{j,\infty}^f(V), \quad (14)$$

for all $j = 1, \dots, n_f$, and freezing ultra-slow variables, that is setting

$$x_j^{us} \equiv \bar{x}_j^{us},$$

for all $j = 1, \dots, n_{us}$, where the values \bar{x}_j^{us} belong to the physiological range of the different variables. The remaining dynamics read as

$$\begin{aligned} \dot{V} &= I_{ion}(V, x_\infty^f(V), x^s, \bar{x}^{us}) + I_{app}, \\ \tau(V)\dot{x}_j^s &= (-x_j^s + x_{j,\infty}^s(V)), \quad j = 1, \dots, n_s \end{aligned}$$

which is a fast-slow system with V as fast variable and x^s as slow variables.

The planar reduction proceeds from the change of variables

$$\begin{aligned} n &= x_1^s, \\ n_i^\perp &= x_i^s - x_{i,\infty}^s(n_\infty^{-1}(n)), \quad i = 2, \dots, n_s, \end{aligned}$$

This change of variable is globally invertible by monotonicity of the (in)activation functions $x_{i,\infty}^s$. Under the additional simplifying assumption of identical time constants

$$\tau_{x_j^s}(V) = \tau(V) \geq \epsilon^{-1} \gg 1, \quad (15)$$

for all $V \in \mathbb{R}$ and all $j = 1, \dots, n_s$, it is an easy calculation to show that

$$\tau(V^*)\dot{n}_i^\perp = -n_i^\perp + \mathcal{O}((n - n^*)^2, (n - n^*)(V - V^*), (V - V^*)^2)$$

around any equilibrium $(V^*, (x_i^s)^*) := (V^*, x_{i,\infty}^s(V^*))$. It follows that, locally around *any* equilibrium, the two dimensional manifold

$$\begin{aligned} \mathcal{M}_{red} &:= \{(V, x_\infty^s) \in \mathbb{R} \times [0, 1]^{n_s} : n_i^\perp = 0, i = 2, \dots, n_s\} \\ &= \{(V, x_\infty^s) \in \mathbb{R} \times [0, 1]^{n_s} : x_i^s = x_{i,\infty}^s(n_\infty^{-1}(n)), i = 2, \dots, n_s\} \end{aligned}$$

is exponentially attractive.

It should be stressed that the (harsh) simplifying assumption (15) is necessary only around the steady-state value V^* and that the hyperbolic decomposition is robust to small perturbations ?. It should also be observed that the proposed two-dimensional reduction is a straightforward generalization of the classical two-dimensional reduction of Hodgkin-Huxley model ?? that rests on setting sodium activation to steady state ($m_{Na} \equiv m_{Na,\infty}(V)$) and using an algebraic relationship between the sodium inactivation and the potassium activation (usually in the form $h \simeq 1 - n$).

4.2 The winged cusp planar model (7) is a local normal form of slow-fast conductance based models

Given an equilibrium $(V^*, n_\infty(V^*))$ of (13), consider the (linear) change of variables

$$\begin{aligned} x &= V - V^* \\ y &= \frac{n - n_\infty(V^*)}{\frac{\partial n_\infty}{\partial V}(V^*)} \end{aligned}$$

The y dynamics is particularly simple. Indeed, by simple Taylor expansion,

$$\begin{aligned}\dot{y} &= \varepsilon(x - y) + \mathcal{O}(x^2), \\ \varepsilon &:= \frac{1}{\tau(V^*)} \ll 1.\end{aligned}$$

In the new coordinates, (13) reads

$$\dot{x} = F\left(x + V^*, n_\infty(V^*) + \frac{\partial n_\infty}{\partial V}(V^*)y\right) + I \quad (16a)$$

$$\dot{y} = \varepsilon(x - y) + \mathcal{O}(x^2). \quad (16b)$$

Simple computations show that (16a) satisfies

$$\begin{aligned}\frac{\partial \dot{x}}{\partial x}(0, 0) &= \frac{\partial I_{ion}}{\partial V} + \sum_{i=1}^{n_f} \frac{\partial I_{ion}}{\partial x_i^f} \frac{\partial x_{i,\infty}^f}{\partial V} \\ \frac{\partial \dot{x}}{\partial y}(0, 0) &= \sum_{i=1}^{n_s} \frac{\partial I_{ion}}{\partial x_i^s} \frac{\partial x_{i,\infty}^s}{\partial V}\end{aligned}$$

where the right hand sides are intended computed at $V = V^*$, $x^f = x_\infty^f(V^*)$, $x^s = x_\infty^s(V^*)$, and $x^{us} = \bar{x}^{us}$.

We claim that the critical manifold $\dot{x} = 0$ of (13) has a degenerate singularity provided that

- (i) the full slow-fast subsystem has a degenerate equilibrium, that is, the Jacobian of the slow-fast subsystem (12a-12c) is singular
- (ii) at such equilibrium, the contributions of slow restorative and slow regenerative channels ? are perfectly balanced, that is

$$\sum_{i=1}^{n_s} \frac{\partial I_{ion}}{\partial x_i^s} \frac{\partial x_{i,\infty}^s}{\partial V} = 0.$$

To prove our claim we notice with similar computations as ? that conditions (i) and (ii) imply that

$$\frac{\partial I_{ion}}{\partial V} + \sum_{i=1}^{n_f} \frac{\partial I_{ion}}{\partial x_i^f} \frac{\partial x_{i,\infty}^f}{\partial V} = 0,$$

which is equivalent to the Jacobian of the fast subsystems (12a-12b) being singular. Hence, when conditions (i) and (ii) are fulfilled,

$$\frac{\partial \dot{x}}{\partial x}(0, 0) = \frac{\partial \dot{x}}{\partial y}(0, 0) = 0. \quad (17)$$

Property (17) ensures that the critical manifold of (16) has a codimension > 0 singularity at the origin (where, as usual, the slow variable y plays the role of the bifurcation parameter). This singularity corresponds to the transcritical bifurcation detected in arbitrary conductance based models in ?. It is indeed proved in ? that conditions (i) and (ii) enforce a transcritical bifurcation in the associated conductance based model.

Algebraically, (17) ensures that, similarly to the bifurcation parameter in the winged cusp universal unfolding (see Section 2.3), y modulates non-monotonically the fast x dynamics. Physiologically, it captures in the reduced model the non-monotone modulation of membrane potential dynamics by slow restorative (providing negative feedback) and slow regenerative (providing positive feedback) ion channels.

We use the algorithm in ? to detect the degenerate dynamics of (16) in arbitrary conductance based models. This construction reveals that the transcritical bifurcation is

part of the transcritical transition variety in the universal unfolding of the winged cusp. The result is sketched in Figure 10 left and verified numerically in the Hodgkin-Huxley model augmented with a calcium current in Figure 10 right. The model and its reduction are presented and further discussed in Section 4.3 below. The obtained phase plane is organized by the mirrored hysteresis bifurcation diagram of the normal form (7) in Fig. 2, in the limiting case in which the two hysteresis branches merge at the transcritical bifurcation. This provides an indirect proof that the global phase plane is organized by the winged cusp. This singularity is indeed the only (codimension ≤ 3) singularity exhibiting the mirrored hysteresis in its universal unfolding (see (?, Section IV.4)).

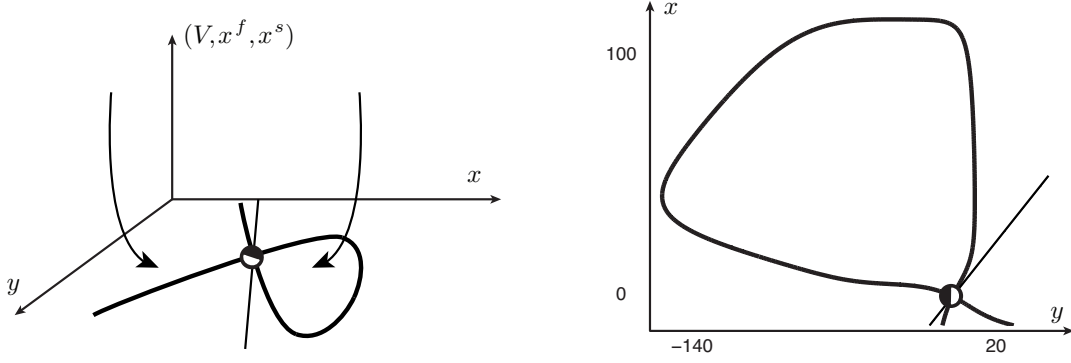


Figure 10: A transcritical bifurcation in the universal unfolding of the winged cusp organizes the dynamics of the two-dimensional reduction of generic conductance based models. Left: Sketch of the dynamics on the two-dimensional invariant manifold \mathcal{M}_{red} . Right: construction of the two dimensional reduction (16) at the transcritical bifurcation in the Hodgkin-Huxley model augmented with a calcium current (18)-(19).

One can push forward the singularity analysis and derive an algorithm to enforce the degenerate conditions of the winged cusp rather than the transcritical bifurcation by using additional model parameters as auxiliary parameters (?, Section III.4). This would lead to the conclusion that the critical manifold of the reduced dynamics (16) is actually a versal unfolding of the winged cusp. Alternatively, one can modulate model parameters and show that their variations recover all persistent bifurcation diagrams of the winged cusp. Such computations are however lengthy and bring no new information to the picture presented here.

4.3 Application to the Hodgkin-Huxley model augmented with a regenerative channel

The first conductance-based model appears in the seminal paper of Hodgkin-Huxley ?

$$C\dot{V} = -\bar{g}_K n^4 (V - V_K) - \bar{g}_{Na} m^3 h (V - V_{Na}) - g_l (V - V_l) + I \quad (18a)$$

$$\tau_m(V) \dot{m} = -m + m_\infty(V) \quad (18b)$$

$$\tau_n(V) \dot{n} = -n + n_\infty(V) \quad (18c)$$

$$\tau_h(V) \dot{h} = -h + h_\infty(V), \quad (18d)$$

where the time constants τ_x and the steady state characteristics x_∞ , $x = m, n, h$ are chosen in accordance with the original model (see Appendix D). The model only accounts for two ionic currents: sodium, with its fast activation variable m and slow inactivation h , and potassium, with slow activation n . The classical phase portrait reduction ?? is obtained with the quasi-steady state approximation $m \simeq m_\infty(V)$ and the empirical fit $h \simeq 1 - n$. It is well known that in its physiological part ($0 < n < 1$) this phase portrait is qualitatively the FitzHugh phase portrait in Fig. 1. But we showed in (?, Figure 5) that the entire phase portrait ($n \in \mathbb{R}$) indeed also contains the “mirrored” phase portrait of Fig. 2. This

observation suggests that a winged cusp organizes the fast subsystem (18a-18b) of Hodgkin-Huxley dynamics. The singularity is found in a non-physiological range of the phase space ($n < 0$), which is consistent with the absence of slow regenerative currents in the model.

The missing element in Hodgkin-Huxley model to make the winged cusp physiological is a slow regenerative ion channel. Following ?, we add the calcium current

$$I_{Ca,L} = -\bar{g}_{Ca}d(V - V_{Ca}) \quad (19a)$$

$$\tau_d(V)\dot{d} = -d + d_\infty(V). \quad (19b)$$

The algorithm in ? detects a transcritical bifurcation for

$$V^* \simeq -61.2730, \quad g_{Ca}^* \simeq 0.2520, \quad I^* \simeq -30.7694.$$

Following the construction in Section 4.2, in particular, Eq. (16), the associated reduced variational dynamics at the transcritical bifurcation reads

$$\begin{aligned} \dot{x} = & -\bar{g}_K \left(n_\infty(V^*) + y \frac{\partial n_\infty}{\partial V}(V^*) \right)^4 (V^* + x - V_K) \\ & -\bar{g}_{Na}m_\infty(V^* + x)^3 \left(h_\infty(V^*) + y \frac{\partial h_\infty}{\partial V}(V^*) + \mathcal{O}(y^2) \right) (V - V_{Na}) \\ & -\bar{g}_{Ca}^* \left(d_\infty(V^*) + y \frac{\partial d_\infty}{\partial V}(V^*) + \mathcal{O}(y^2) \right) (V - V_{Ca}) \\ & -g_l(V - V_l) + I^* \\ \dot{y} = & \varepsilon(x - y) + \mathcal{O}(x^2). \end{aligned}$$

Its phase plane is drawn in Figure 10 right.

We now apply the global two-dimensional reduction described in Section 4.1, in particular, Eq. (13), to model (18-19). To this aim, we express all variables in terms of potassium activation n . Since in the original model its activation function cannot be explicitly inverted, we use the exponential fitting

$$n_\infty(V) = \frac{1}{1 + e^{0.06(11.6-V)}}, \quad n_\infty^{-1}(n) = 11.6 - \frac{1}{0.06} \ln \left(\frac{1}{n} - 1 \right)$$

Figure 11 provides a comparison of the behavior of the original and reduced models. Despite quantitative differences (in particular, as in the reduction of the original Hodgkin-Huxley model, treating fast variables as instantaneous increases spiking frequency), the reduced model faithfully captures the qualitative behavior of its high-dimensional counterpart, for instance, rest-spike bistability. Phase plane analysis of the associated normal form (7) provides a clear geometrical interpretation of such dynamical behavior (Fig. 2).

4.4 The role of ultra-slow variables

Ultra-slow variables appear in a variety of forms: ultra-slow gating variables (e.g. inactivation of calcium channels), intracellular calcium (e.g. SK channels), metabotropic regulation of channel expression (e.g. regulation of calcium channel expression by serotonin receptors), homeostatic regulation of channel expression (e.g. calcium dependent expression of ion channels), etc. . As such, they do not allow a systematic analysis as for slow-gating variables. However, their effect on the model reduction (13) can be understood in terms of modulation of the unfolding parameters of the associated normal form. The observation that the many (auxiliary) parameters of conductance based models might naturally provide a versal unfolding of the winged cusp organizing their fast critical manifold suggests that variations in ultra-slow variables act as ultra-slow modulation of the unfolding parameters in the associated normal form. The effect of ultra-slow variables is thus constrained to

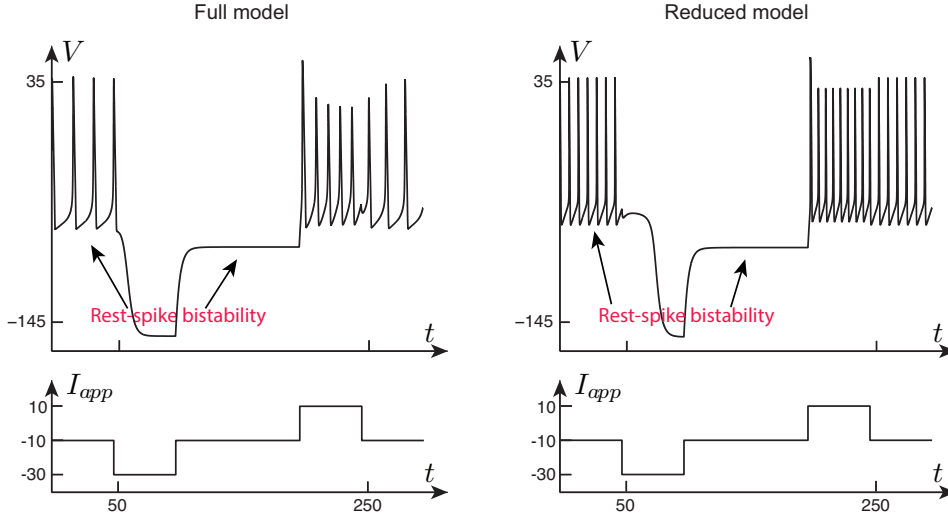


Figure 11: Comparison of the full Hodgkin-Huxley augmented with a calcium current (18)-(19) and its two-dimensional reduction, obtained by applying the reduction procedure of Section 4.1.

reshape the geometry of the slow fast phase portrait. This might lead to ultra-slow adaptation mechanisms (similarly to the action of α in Fig. 4) or to even slower modulation mechanisms (similarly to the action of k and V_0 in Fig. 12 below).

Clearly, this does not permit to conclude precise results on the global dynamics of a multi-timescale model, but suggest that the low dimensional bursting modulation mechanism described here has a strong relevance for generic conductance-based models.

5 Modulation of bursting by unfolding parameters and its physiological interpretation

5.1 Bursting modeling and unfolding theory

The rich literature on mathematical modeling of bursting calls for a few comparisons with the model proposed in the present paper. The geometry of our bursting attractor is the most classical one of a saddle-homoclinic burster (one out of the 16 bursting attractors in the recent classification of Izhikevich, see (?, page 376)). Such an attractor is for instance found in the early bursting model of Hindmarsh and Rose ?. The two models exhibit an analog geometry: the mirror of the classical Fitz-Hugh phase portrait, obtained here by mirroring the fast variable cubic nullcline, is obtained there by mirroring the monotone activation function of the recovery variable. But the Hindmarsh-Rose model lacks the organization of some high-codimension singularity, making it impractical for modulation studies (see, e.g., ?) and for physiological interpretability.

The more recent literature on bursting has certainly exploited unfolding theory around high-codimension bifurcations to construct different types of bursting attractors. A non exhaustive list is ???? and the references discussed in (?, page 376). The outcome of those studies is a useful mathematical classification between different bursting attractors organized by different bifurcations but it is not clear how to use this classification for modulation studies. A possible reason is that most of those references construct bursting models from restorative phase portraits that retain the qualitative organization of Fitz-Hugh model by a hysteresis singularity. Such models lack the transcritical bifurcation that organizes the normal form reduction of general bursting conductance based models.

The approach of the present paper differs from earlier studies in starting from the cusp singularity, inspired by our original observation that the mirrored hysteresis phase portrait

organizes the reduced Hodgkin-Huxley dynamics (Fig. 5). The direct link between the mathematical unfolding of the cusp singularity and the local normal form of conductance-based models in the vicinity of their transcritical bifurcation is probably crucial in using unfolding theory to understand the modulation of bursting in neuronal models.

5.2 A geometrical and physiological modulation of a burster across bursting types

The single geometric attractor of (11) contains a continuum of different bursting wave forms modulated by the bifurcation and the unfolding parameters. Beyond the route to bursting studied in Section 3, Figure 12 illustrates a situation where the bifurcation parameter and the affine unfolding parameters are fixed but where the two remaining unfolding parameters are modulated in a quasi static manner. The figure displays a variety of waveforms that nevertheless share the same geometry of the bursting attractor as hysterethic paths in the universal unfolding of the winged cusp. For small autocatalytic feedback gain k , corresponding to low expression of fast sodium channels, the model emits small oscillatory potentials (SOP), on the left. Increasing this gain, the waveform smoothly evolves toward a classical “square-wave” oscillation, on the right, after a transient “tapered” bursting activity, shown in the inset (see (Fig. 12, page 376) and references therein for a discussion about the different bursting types). As in the case of the route from tonic spiking to bursting, the transition shown in Fig. 12 has physiological relevance. For instance, a similar transition has been observed during development of neuronal cells (Fig. 12).

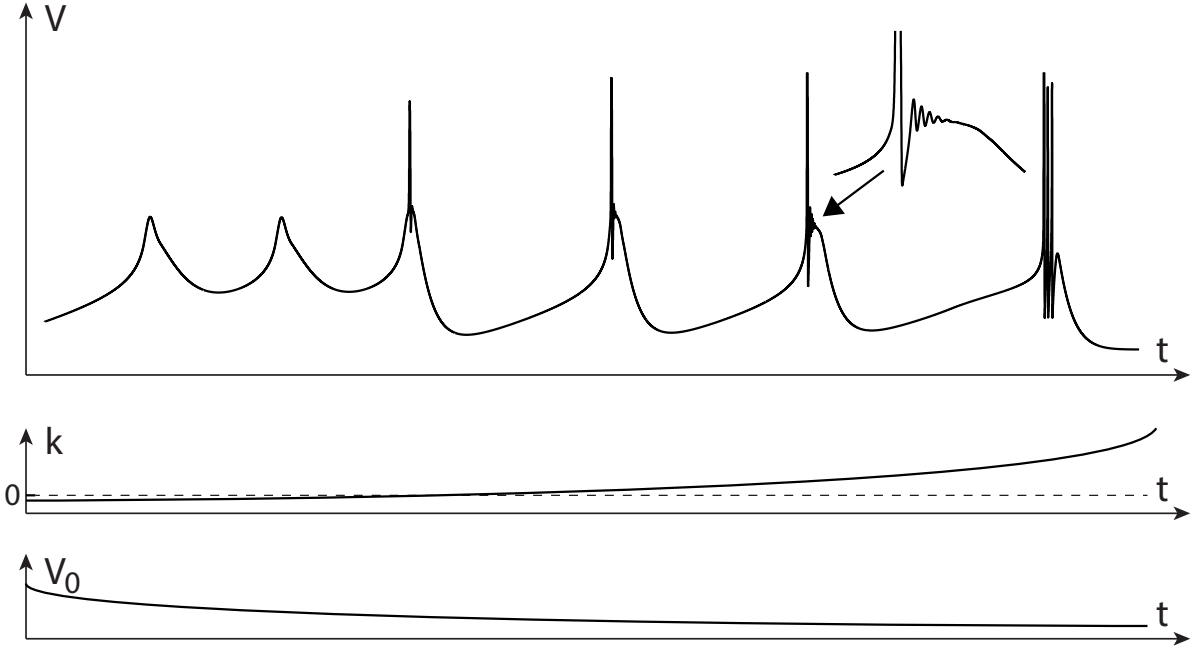


Figure 12: **Modulation of model (11) across different bursting wave forms.** Increasing the fast positive feedback gain k and decreasing the half-activation potential V_0 the model smoothly evolves from (calcium driven) small oscillatory potentials SOP (on the left) to “square-wave”-like bursting (on the right) across “tapered”-like bursting (shown in the inset). Parameters values are provided in Section C.

The geometry of the “tapered”-like bursting wave-form in Figure 12 reveals another subtlety of the winged cusp unfolding. In addition to broad regions of restorative and regenerative excitability, Fig. 8A shows a small parametric region of mixed excitability (type V in the terminology of (Fig. 8)). Like regenerative phase portraits, phase portraits in this region have a persistent bistable range, but it is of fold/fold type, with a down-state that is a regenerative fixed point and an up-state that is either a restorative fixed point or a limit

cycle (emerging from a Hopf bifurcation within or outside the bistable range). The bursting attractor observed in this region can be considered as a variant of the bursting attractor associated to regenerative excitability. Both bursting attractors share the same geometry of hysteretic paths in the unfolding of the winged cusp singularity but the fold/fold variant exhibits the peculiar wave form illustrated in Fig. 13, usually studied under the name of “tapered” bursting in the literature, see e.g. (? , page 376).

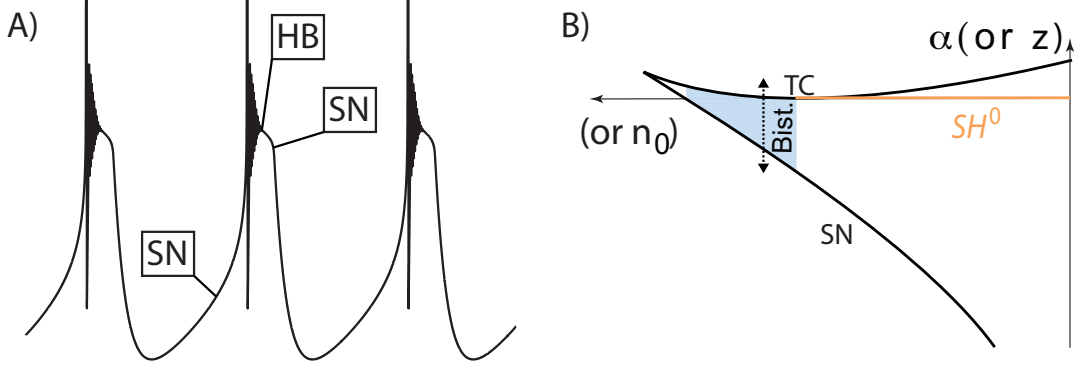


Figure 13: **Variant of the saddle-homoclinic bursting attractor in model (11).** **A.** When the fast-slow subsystem (11a-11b) exhibits Type V excitability ?, the bistable range is of fold / fold type leading to a “tapered” bursting waveform. Parameters values are provided in Section C. **B.** The hysteretic path associated to this type appears along path *ii*) of Fig. 8. At the two ends of the bistable range, the up and down attractors are stable equilibria losing stability in a saddle-node bifurcation. Depending on the excitability subtype, the burst onset can either exhibit damped spiking oscillations ending in a Hopf bifurcation within the bistable range (a situation captured by the bifurcation diagram in (? , Fig. 5.2)) or a single action potential (a situation captured by the bifurcation diagram in (? , Fig. 5.3)).

It is remarkable that the four different wave forms shown in Figs. 12 and Fig. 13 can be modeled by the same geometric attractor. A companion paper in preparation further investigates the physiological mechanisms that modulate the bursting wave within the unfolding of the winged cusp singularity.

6 Conclusions

The paper proposes that conductance based models exhibiting bursting attractors are organized by a winged cusp singularity. The geometry of the resulting attractor is classical (a hysteretic modulation of a slow-fast portrait over a rest-spike bistable range) but singularity theory is used to identify key parameters for the modulation of the bursting attractor.

The cusp singularity organizes the slow-fast phase portrait around the mirror hysteresis of Section 2.3 in contrast to the standard hysteresis of classical phase portrait reductions of Hodgkin-Huxley model.

The bifurcation parameter has the convenient physiological interpretation of a ionic balance recently studied in ?. Its modulation through the transcritical variety of the cusp unfolding governs a geometric transition from tonic spiking to bursting in the three-timescale normal form (9): it provides a physiologically relevant route to bursting.

The affine unfolding parameter has the physiological interpretation of an ultraslow ionic current, typically driven by the intracellular calcium concentration. Its modulation provides the classical adaptation variable of the three time-scale bursting attractor.

The two remaining unfolding parameters have the physiological interpretation of a fast autocatalytic gain (the maximal sodium conductance) and of an average half activation potential, respectively. Their quasi static modulation evolves the bursting attractor across different bursting wave forms, consistently with what is observed experimentally in neuronal development, for instance.

In spite of the vast diversity of ion channels encountered in different neurons and the resulting vast diversity of regulation pathways, singularity theory and time scale separation suggest an apparent simplicity and universality in the underlying modulation mechanisms, as paths in the universal unfolding of the winged cusp. Those features are appealing to address system theoretic questions such as sensitivity, robustness, and homeostasis issues.

7 Acknowledgments

Prof. M. Golubitsky is gratefully acknowledged for insightful comments and suggestions during the visit of the first author at the Mathematical Bioscience Institute (Ohio State University).

A Codimension 1 and 2 bifurcation varieties in (7)

The fixed point equation of (7) is organized by a winged cusp at $x_{w\text{cusp}} := \frac{1}{3}$, $\lambda_{w\text{cusp}} := 0$, $\alpha_{w\text{cusp}} := -\frac{1}{27}$, $\beta_{w\text{cusp}} := -\frac{1}{3}$, $\gamma_{w\text{cusp}} := -2$. Codimension 1 transcritical and hysteresis bifurcation transition varieties in its unfolding are defined by

$$\alpha_{TC}(\beta, \gamma) = -\bar{x}_{TC}^3 - (\bar{\lambda}_{TC} + \bar{x}_{TC})^2 + \beta\bar{x}_{TC} - \gamma\bar{x}_{TC}(\bar{\lambda}_{TC} + \bar{x}_{TC}) \quad (20)$$

with

$$\bar{x}_{TC}(\beta, \gamma) = \frac{\gamma^2 - (\gamma^4 + 48\beta)^{1/2}}{12} \quad (21a)$$

$$\bar{\lambda}_{TC}(\beta, \gamma) = -\frac{\bar{x}_{TC}(2 + \gamma)}{2} \quad (21b)$$

and

$$\alpha_{HY}(\beta, \gamma) = -\bar{x}_{HY}^3 - (\bar{\lambda}_{HY} + \bar{x}_{HY})^2 + \beta\bar{x}_{HY} - \gamma\bar{x}_{HY}(\bar{\lambda}_{HY} + \bar{x}_{HY}) \quad (22)$$

with

$$\bar{x}_{HY}(\gamma) = -\frac{1 + \gamma}{3} \quad (23a)$$

$$\bar{\lambda}_{HY}(\beta, \gamma) = \frac{\beta - 3\bar{x}_{HY}^2 - \bar{x}_{HY}(2 + 2\gamma)}{2 + \gamma} \quad (23b)$$

respectively.

The codimension 2 pitchfork variety is defined by

$$\gamma_{PF}(\beta) = \left(3\beta + \left(9\beta^2 + \frac{1}{27} \right)^{1/2} \right)^{1/3} - \frac{1}{\left(3\beta + \left(9\beta^2 + \frac{1}{27} \right)^{1/2} \right)^{1/3}} - 1 \quad (24a)$$

$$\alpha_{PF}(\beta) = -\bar{x}_{PF}^3 - (\bar{\lambda}_{PF} + \bar{x}_{PF})^2 + \beta\bar{x}_{PF} - \gamma_{PF}\bar{x}_{PF}(\bar{\lambda}_{PF} + \bar{x}_{PF}) \quad (25)$$

with

$$\bar{x}_{PF}(\beta) = -\frac{1 + \gamma_{PF}}{3} \quad (26a)$$

$$\bar{\lambda}_{PF}(\beta) = \frac{\beta - 3\bar{x}_{PF}^2 - \bar{x}_{PF}(2 + 2\gamma_{PF})}{2 + \gamma_{PF}} \quad (26b)$$

B Proofs

B.1 Proof of Theorem 2

We rely on geometric singular perturbation arguments ??????. The reduced dynamics associated to (7), evolving on the slow time scale $\tau = \varepsilon t$, is given by

$$0 = G_{w\text{cusp}}^s(x, \lambda + y; \alpha, \beta, \gamma) \quad (27a)$$

$$\dot{y} = x - y, \quad (27b)$$

whereas the associated layer dynamics, evolving on the fast time scale t , is given by

$$\dot{x} = G_{w\text{cusp}}^s(x, \lambda + y; \alpha, \beta, \gamma) \quad (28a)$$

$$\dot{y} = 0. \quad (28b)$$

We construct the singular bistable phase portrait starting from the degenerate situation in Fig. 3 center, corresponding to a pitchfork bifurcation. The same qualitative phase

portrait is obtained on the pitchfork variety (24) for all $\beta > \beta_{wucusp}$. Perturbing γ out of the pitchfork variety, but remaining on the transcritical variety defined by (20), the phase portrait perturbs to one of the two qualitative situations in Fig. 3 center - top or bottom. Finally, for λ below and sufficiently near $\lambda_{TC}(\beta, \gamma)$ and α below and sufficiently near $\alpha_{TC}(\beta, \gamma)$ one obtains the qualitative slow-fast dynamics in Fig. 14A, which leads to the singular phase-portrait in Fig. 14B. The following lemma summarizes this construction.

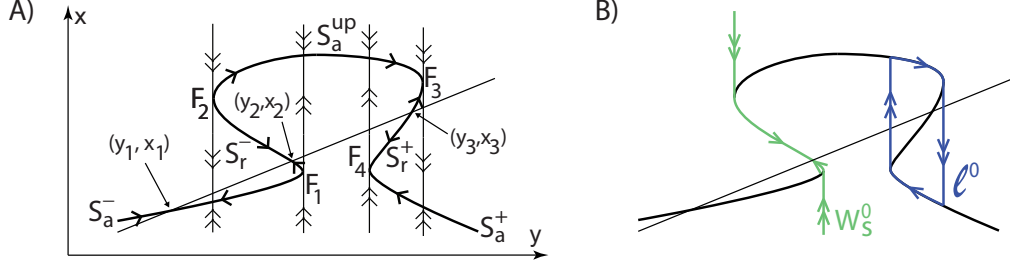


Figure 14: Slow fast dynamics associated to (27-28).

Lemma 1 For all $\beta > \beta_{wucusp}$, there exists $\Delta_\gamma > 0$ such that, for all $\gamma \in (\gamma_{PF}(\beta) - \Delta_\gamma, \gamma_{PF}(\beta) + \Delta_\gamma)$, there exists $\Delta_\lambda > 0$ such that, for all $\lambda \in (\bar{\lambda}_{TC}(\beta, \gamma) - \Delta_\lambda, \bar{\lambda}_{TC}(\beta, \gamma))$, there exists $\Delta_\alpha > 0$ such that, for all $\alpha \in (\alpha_{TC}(\beta, \gamma) - \Delta_\alpha, \alpha_{TC}(\beta, \gamma))$, the following hold (refer to Fig. 14 - left for the notation):

- i) The critical manifold of the slow-fast dynamics (27-28) has a mirrored hysteresis shape. In particular, it is composed of the attractive branches S_a^- , S_a^+ , and S_a^{up} , the repelling branches S_r^- and S_r^+ , and the four folds F_i , $i = 1, \dots, 4$, connecting them.
- ii) There are exactly three nullcline intersection (y_i, x_i) , $i = 1, \dots, 3$, belonging to S_a^- , S_r^- , and S_r^+ , respectively.

A direct geometric inspection reveals the presence of a singular periodic orbit ℓ^0 and a singular saddle separatrix W_s^0 . These objects persist for $\epsilon > 0$, as proved in the following lemma, which proves Theorem 2.

Lemma 2 Let (y_i, x_i) , $i = 1, \dots, 3$ be defined as in the statement of Lemma 1 ii). For all $\lambda, \alpha, \beta, \gamma$ satisfying conditions of Lemma 1, there exists $\bar{\epsilon}$ such that, for all $\epsilon \in (0, \bar{\epsilon})$

- i) (y_1, x_1) is locally exponentially stable, (y_2, x_2) is a hyperbolic saddle, and (y_3, x_3) is locally exponentially unstable.
- ii) There exists an exponentially stable relaxation oscillation limit cycle ℓ^ϵ surrounding (y_3, x_3) .
- iii) The stable manifold W_s^ϵ of (y_2, x_2) separates the basin of attraction of (y_1, x_1) and ℓ^ϵ .

Proof of Lemma 2.

i) From Lemma 1, the fixed point (y_1, x_1) belongs to the attractive branch S_a^- of the critical manifold \mathcal{S} . Moreover, it is an exponentially stable fixed point of the reduced dynamics (27). From standard persistence arguments ?, there exists $\bar{\epsilon}_1$ such that, for all $\epsilon \in (0, \bar{\epsilon}_1]$, (y_1, x_1) is an exponentially stable fixed point of (7). The fixed point (y_2, x_2) belongs to the repelling branch S_r^- of the critical manifold \mathcal{S} . Moreover, it is an exponentially stable fixed point of the reduced dynamics (27). Again from ?, there exists $\bar{\epsilon}_2$ such that, for all $\epsilon \in (0, \bar{\epsilon}_2]$, there exists an exponentially unstable local invariant manifold $W_{s,loc}^\epsilon$ such that all trajectories starting in $W_{s,loc}^\epsilon$ approach (y_2, x_2) exponentially fast. $W_{s,loc}^\epsilon$ is the local stable manifold of (y_2, x_2) . Its unstable manifold is given by the fiber of the unstable manifold of $W_{s,loc}^\epsilon$ passing through (y_2, x_2) . The fixed point (y_3, x_3) belong to the repelling branch S_r^+ of the critical manifold \mathcal{S} , moreover it is an exponentially

unstable fixed point of the reduced dynamics (27). By ?, there exists $\bar{\varepsilon}_3 > 0$ such that, for all $\epsilon \in (0, \bar{\varepsilon}_3]$, (y_3, x_3) is an exponentially unstable fixed point of (7).

ii) The slow fast dynamics possesses a singular periodic orbit ℓ^0 (See Fig. 14). Following ?, there exists $\bar{\varepsilon}_4$ such that, for all $\epsilon \in (0, \bar{\varepsilon}_4]$, there exists an exponentially stable relaxation oscillation limit cycle ℓ^ϵ surrounding (y_3, x_3) .

iii) In backward time, trajectories of the reduced dynamics (27) starting on \mathcal{S}_r^- in a neighborhood of (y_2, x_2) approach either the fold \mathcal{F}_1 or the fold \mathcal{F}_2 . Following ?, there exists $\bar{\varepsilon}_5$ such that, for all $\epsilon \in (0, \bar{\varepsilon}_5]$, all trajectories starting in the local stable manifold $W_{s,loc}^\epsilon$ approach (in backward time) either the fold \mathcal{F}_1 or the fold \mathcal{F}_2 along an invariant manifold W_s^ϵ , which continues after the fold singularities roughly parallel to trajectories of the layer problem. Therefore, the branch that continues after \mathcal{F}_1 extends to $x = -\infty$, whereas the branch that continues after \mathcal{F}_2 extends to $x = +\infty$. The invariant manifold W_s^ϵ is the saddle stable manifold and separates the plane in two disconnected regions that contain, respectively, the two attractors (y_1, x_1) and ℓ^ϵ .

Items *i)*, *ii)*, and *iii)* are proved by picking $\bar{\varepsilon} = \min_{i=1,\dots,5} \bar{\varepsilon}_i$. □

□

B.2 Proof of Theorem 3

Starting from a set of parameter satisfying the condition of Lemma 1 and increasing α to $\alpha = \alpha_{TC}(\beta, \gamma)$ the two folds F_1 and F_4 in Fig. 14A approach each other and eventually collide in a transcritical singularity TC , as in the slow-fast dynamics in Figure 15A. A direct geometrical inspection reveals the presence of a singular saddle-homoclinic trajectory SH^0 (Fig. 15B) for which the transcritical singularity serves as connecting point. This homoclinic orbit persists for $\varepsilon > 0$, as sketched in Figure 16A. On the contrary, decreasing α the two folds move away from each other until the left branch of the mirrored hysteresis is tangent to the y nullcline at a saddle-node bifurcation SN and eventually remains on its left, as in Fig. 16B. The following lemma summarizes this analysis. For its statement, we refer to Figures 14 and 15.

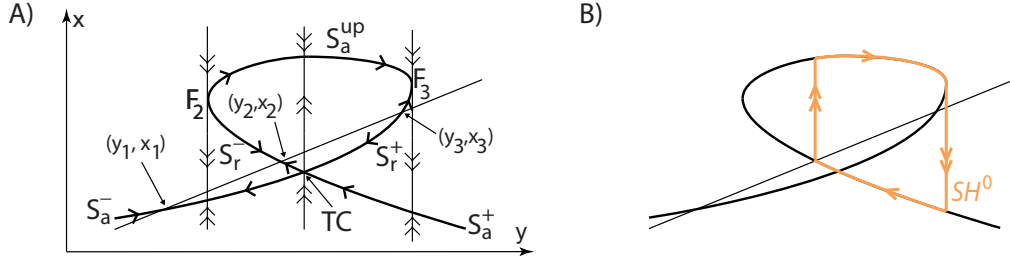


Figure 15: Slow fast dynamics associated to (27-28).

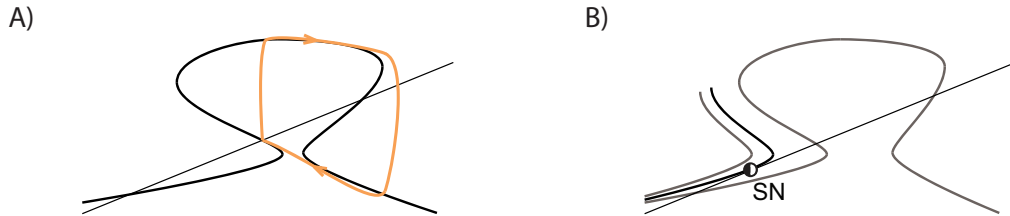


Figure 16: **Phase portrait of (7), with parameters and the function y_∞ satisfying conditions of Lemma 3.** **A.** Singularly perturbed saddle-homoclinic trajectory for $\alpha = \alpha_{SH}^0 + \alpha_c(\sqrt{\varepsilon})$. **B.** Saddle-node bifurcation.

Lemma 3 For all $\beta > \beta_{wusp}$, there exists $\Delta_\gamma > 0$ such that, for all $\gamma \in (\gamma_{PF}(\beta) - \Delta_\gamma, \gamma_{PF}(\beta) + \Delta_\gamma)$, there exist $\Delta_\lambda > 0$ such that, for all $\lambda \in (\bar{\lambda}_{TC}(\beta, \gamma) - \Delta_\lambda, \bar{\lambda}_{TC}(\beta, \gamma))$, there exists $\bar{\varepsilon} > 0$, such that, for $\varepsilon \in (0, \bar{\varepsilon}]$ the following hold:

i) Let $\alpha_{SH}^0 := \alpha_{TC}(\beta, \gamma)$. There exists a smooth function $\alpha_c(\cdot)$ defined on $[0, \sqrt{\bar{\varepsilon}}]$, and satisfying $\alpha_c(0) = 0$ and $\alpha_c(\sqrt{\varepsilon}) < 0$, for all $\varepsilon \in (0, \bar{\varepsilon}]$, such that, for $\alpha = \alpha_{SH}^\varepsilon := \alpha_{SH}^0 + \alpha_c(\sqrt{\varepsilon})$, (7) has an unstable saddle-homoclinic orbit SH^ε .

ii) For all $\varepsilon > 0$, there exists $\alpha_{SN} < \alpha_{SH}^0$ such that (7) has a non-degenerate saddle-node bifurcation for $\alpha = \alpha_{SN}$ at which the node (y_1, x_1) and the saddle (y_2, x_2) merge.

iii) For all $\alpha \in [\alpha_{SN}, \alpha_{SH}^0]$ the nullcline intersection (y_3, x_3) belongs to the repelling branch S_r^+ (where S_r^+ is defined as in Figure 14A).

iv) For all $\alpha \in [\alpha_{SN}, \alpha_{SH}^\varepsilon]$, there exists an exponentially stable relaxation oscillation limit cycle ℓ^ε surrounding (y_3, x_3) .

v) There exists $\alpha_{FLC}^\varepsilon \in (\alpha_{SH}^\varepsilon, \alpha_{SH}^0)$ such that, for $\alpha = \alpha_{FLC}^\varepsilon$, the family P^ε of stable periodic orbits merge at a fold limit cycle bifurcation with the family of unstable periodic orbits Q^ε emerging from the unstable saddle-homoclinic bifurcation.

Proof of Lemma 3. i) For γ in a neighborhood of $\gamma_{PF}(\beta)$, $\alpha = \alpha_{TC}(\beta, \gamma)$ and λ smaller than and sufficiently near to $\bar{\lambda}_{TC}(\beta, \gamma)$, there are exactly three nullcline intersections (y_i, x_i) , $i = 1, 2, 3$, belonging to the attractive branch S_a^- , the repelling branch S_r^- , and the repelling branch S_r^+ , respectively. Relying on the results in ? and following exactly the same steps as (? , Section 6.1), we can find ε_1 , such that the existence part of the point i) holds with $\bar{\varepsilon} = \varepsilon_1$. The resulting saddle-homoclinic trajectory is sketched in Fig. 16A. To prove that such homoclinic trajectory is unstable, recall that the stability of a saddle-homoclinic orbit is determined by the saddle quantity σ , that is, the trace of the Jacobian computed at the saddle and at the saddle-homoclinic bifurcation: if $\sigma > 0$ (resp. $\sigma < 0$) the homoclinic orbit is unstable (resp. stable). The Jacobian J_{SH} of (7) computed at (y_2, x_2) at the saddle-homoclinic bifurcation has the form

$$J_{SH} = \begin{pmatrix} a & b \\ \varepsilon c & -\varepsilon d \end{pmatrix}, \quad a, d > 0, \quad b, c \in \mathbb{R}.$$

Therefore the saddle quantity $\sigma = a - \varepsilon d > 0$, for all $0 < \varepsilon < a/d$.

ii) For γ in a neighborhood of $\gamma_{PF}(\beta)$, $\alpha = \alpha_{TC}(\beta, \gamma)$, and λ smaller than and sufficiently near to $\bar{\lambda}_{TC}(\beta, \gamma)$, the (cubic) fixed point equation $G_{wusp}(x, \lambda + x; \alpha, \beta, \gamma)$ has three roots, corresponding to the three fixed point (y_i, x_i) , $i = 1, 2, 3$ of point i). Decreasing α , the two smaller roots (corresponding to the fixed point (y_1, x_1) and (y_2, x_2)) approach each other and eventually merge in a quadratic zero for $\alpha = \alpha_{SN}$ corresponding to a non-degenerate saddle-node bifurcation.

iii) We prove the statement for $\gamma = \gamma_{PF}(\beta)$ since, by continuity, the same will hold in a neighborhood. When $\gamma = \gamma_{PF}(\beta)$, $\alpha = \alpha_{PF}(\beta)$, and λ is smaller than and sufficiently near to $\bar{\lambda}_{PF}(\beta)$, the nullcline intersection (y_3, x_3) lies on S_r^+ . By continuity, the same is true for all α close to $\alpha_{PF}(\beta)$. Since the value $\alpha_{SN} \uparrow \alpha_{PF}(\beta)$ continuously as $\lambda \uparrow \bar{\lambda}_{PF}(\beta)$, one can pick λ sufficiently close to $\bar{\lambda}_{PF}(\beta)$ such that (y_3, x_3) lies on S_r^+ for all $\alpha \in [\alpha_{SN}, \alpha_{PF}(\beta))$.

iv) By points ii) and iii) above and the same arguments as the proof of point ii) in Lemma 3, we can find $\varepsilon_2 > 0$ such that, for all $\varepsilon \in (0, \min(\varepsilon_1, \varepsilon_2))$, where ε_1 is defined as in the proof of point i) above, and all $\alpha \in [\alpha_{SN}, \alpha_{SH}^\varepsilon)$, there exists a periodic orbit ℓ^ε surrounding (y_3, x_3) and, moreover, this periodic orbit is exponentially stable. For $\alpha = \alpha_{SH}^\varepsilon$, the stable periodic orbit co-exist with the unstable homoclinic orbit, since by (? , Theorem 3.5), a branch of stable periodic orbits cannot end at an unstable homoclinic bifurcation.

v) The existence of $\alpha_{FLC}^\varepsilon \in (\alpha_{SH}^\varepsilon, \alpha_{SH}^0)$ satisfying the statement follows by two main observations. First, again by (? , Theorem 3.5) there exists a family Q^ε of unstable periodic orbits emergenging at $\alpha = \alpha_{SH}^\varepsilon$ from the unstable homoclinic bifurcation. Second, simple geometric arguments show that for $\alpha = \alpha_{SH}^0$ (and ε sufficiently small) no periodic orbit can

exists. The existence of the fold limit cycle bifurcation then follows by noticing that the fold limit cycle is the only planar bifurcation of periodic orbits not involving a Hopf point and that both the unstable homoclinic bifurcation and the fold limit cycle bifurcation are generically found in the unfolding of the degenerate situation in which the saddle quantity σ is zero, corresponding to a resonant homoclinic orbit. The unfolding of this bifurcation, also called resonant side-switching, is detailed in (?, Theorem A). \square

Figure 17 summarizes the results in Lemma 3.

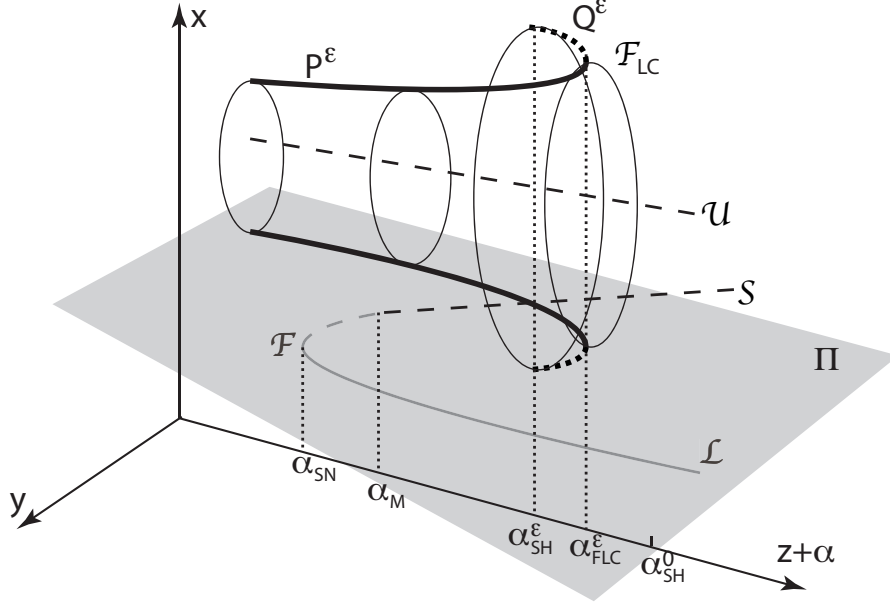


Figure 17: **Bifurcation diagram of (9a-9b) with respect to z and parameters satisfying condition of Lemma 3.** See the main text describing Fig. 5 for the notation.

We now follow ?? to derive suitable conditions on the four parameters a, b, c in (9c) such that z hysteretically modulates (9a-9b) along its rest spike bistable range. To this aim, note that the minimum value of y along the family of singular periodic orbits ℓ^0 and the singular homoclinic trajectory SH^0 for $\alpha \in [\alpha_{SN}, \alpha_{SH}^0]$ (see Figure 4) is necessarily strictly larger than the maximum value of y along the branch of stable fixed points \mathcal{L} and at the saddle-node bifurcation \mathcal{F} . By persistence arguments, the same holds true in the nonsingular case for ε sufficiently small. It follows that there exists a plane Π in the three-dimensional space x, y, z that, for $\alpha \in [\alpha_{SN}, \alpha_{SH}^0]$, never intersects the family of stable periodic orbits P^ε and the branch of stable fixed points \mathcal{L} , and that intersects once the branch of saddle points \mathcal{S} , say, for $\alpha = \alpha_M$ (see Fig. 17). Clearly, Π splits \mathbb{R}^3 in two open half-spaces. Let Π_ℓ^c be the half space containing the family of singular periodic orbits. Then we pick a, b, c such that $\Pi = \{(x, y, z) : -z + ax + by + c = 0\}$ and $-z + ax + by + c > 0$, for $(x, y, z) \in \Pi_\ell^c$. Under these conditions on a, b, c , Theorem 3 follows along the same line as the proofs in ? (for the analysis near the branch of the stable steady states and the “jump up” at the fold bifurcation) and ? (for the analysis near the branch of periodic orbits and the “jump down” at the fold limit cycle bifurcation). \square

C Parameter for numerical simulations in Figs. 6, 7, 12, 13

For the sake of an easy numerical implementation and the reproduction of “nice” time series, we suggest the following piecewise linear approximation of (11)

$$\dot{V} = kV - \frac{V^3}{3} - (n + n_0)^2 + I - z \quad (29a)$$

$$\dot{n} = \varepsilon_n (\hat{n}_\infty(V - V_0) - n) \quad (29b)$$

$$\dot{z} = \varepsilon_z (\hat{z}_\infty(V - V_1) - z) \quad (29c)$$

where

$$\hat{n}_\infty(V - V_0) := \begin{cases} k_-^n (V - V_0) & \text{if } V < V_0, \\ k_+^n (V - V_0) & \text{if } V \geq V_0. \end{cases}$$

with $0 \leq k_-^n < 1$ and $k_+^n > 1$, and

$$\hat{z}_\infty(V - V_1) := \begin{cases} k_-^z (V - V_1) & \text{if } V < V_1, \\ k_+^z (V - V_1) & \text{if } V \geq V_1. \end{cases}$$

with $0 \leq k_-^z < 1$ and $k_+^z > 1$.

Parameters used in Figs. 6 and 7 are $k = 1$, $I = 11/3$, $\varepsilon_n = 0.02$, $\varepsilon_z = 0.0005$, $V_0 = -0.5$, $k_-^n = 0.4$, $k_+^n = 7$, $V_1 = -1$, $k_-^z = 0$, $k_+^z = 50$. The bifurcation parameter is $n_0 = 0.3$ in Figure 6 left and $n_0 = -1.1$ in Fig. 6 right. In Fig. 7 n_0 is linearly (in time) decreased from 0.3 to -1.1 .

Parameters used in Figs. 12A are $n_0 = -1.1$, $I = 11/3$, $\varepsilon_n = 0.02$, $\varepsilon_z = 0.0001$, $k_-^n = 0.9$, $k_+^n = 7$, $V_1 = -1.2$, $k_-^z = 0$, $k_+^z = 100$. The time-varying parameters k and V_0 evolve as $k(t) = -0.5 + 2.5t/T$ and $V_0(t) = -0.5 - 0.75 \min(1, 1.3t/T)$.

Parameters used in Figs. 13A are $n_0 = -0.2$, $k = 0.7$, $I = 11/3$, $\varepsilon_n = 0.02$, $\varepsilon_z = 0.001$, $V_0 = -1.25$, $k_-^n = 0.9$, $k_+^n = 7$, $V_1 = -1.2$, $k_-^z = 0$, $k_+^z = 50$.

D Parameter for numerical simulations of the Hodgkin-Huxley model in Section 4.3

All the parameter and activation and inactivation rates are taken from the original paper ?. The time constants $\tau_x(V)$ and steady state functions $x_\infty(V)$ are related to the activation and inactivation rates $\alpha_x(V)$ and $\beta_x(V)$, $x = m, n, h$, as follows

$$\tau_x(V) = \frac{1}{\alpha_x(V) + \beta_x(V)}, \quad x_\infty(V) = \frac{\alpha_x(V)}{\alpha_x(V) + \beta_x(V)}.$$